AGU PUBLICATIONS

JGR

Journal of Geophysical Research: Solid Earth

RESEARCH ARTICLE
10.1002/2016JB013376

Key Points:
- SP from coastal and inland aquifers in the UK display tidal power spectra, suggesting distinct SP contributions at both sites
- The tidal SP is 2 orders of magnitude larger at the coast and is dominated by electrokinetic and/or exclusion-diffusion potentials
- Borehole-referenced SP data in the coastal aquifer are dominated by ocean tidal processes and could be used to monitor seawater intrusion

Correspondence to:
DJ. MacAllister,
donaldjohn.macallister@strath.ac.uk

Citation:
MacAllister, DJ., M. D. Jackson, A. P. Butler, and J. Vinogradov (2016), Tidal influence on self-potential measurements, *J. Geophys. Res. Solid Earth*, *121*, 8432–8452, doi:10.1002/2016JB013376.

Received 19 JUL 2016
Accepted 7 NOV 2016
Accepted article online 10 NOV 2016
Published online 3 DEC 2016

Tidal influence on self-potential measurements

DJ. MacAllister[1,2,3], M. D. Jackson[1], A. P. Butler[2], and J. Vinogradov[1,4]

[1]Department of Earth Science and Engineering, Imperial College London, London, UK, [2]Department of Civil and Environmental Engineering, Imperial College London, London, UK, [3]Now at Department of Civil and Environmental Engineering, University of Strathclyde, Glasgow, UK, [4]Now at School of Engineering, Kings College, University of Aberdeen, Aberdeen, UK

Abstract Long-term surface and borehole self-potential (SP) monitoring was conducted in the UK Chalk aquifer at two sites. The coastal site is ~1.7 km from the coast, and the inland site is ~80 km from the coast. At both sites, power spectral density analysis revealed that SP data contain the main ocean tidal periodic components. However, the principal lunar component (M_2), the dominant ocean tidal component, was most significant at the coastal site. The M_2 signal in surface-referenced SP data at the inland site was partly due to telluric currents caused by the geomagnetic ocean dynamo. Earth and/or atmospheric tides also contributed, as the SP power spectrum was not typical of a telluric electric field. The M_2 component in borehole-referenced data at the inland site was below the significance level of the analysis method and was 2 orders of magnitude smaller than the M_2 signal in borehole-referenced SP data at the coastal site. The tidal response of the SP data in the coastal borehole is, therefore, primarily driven by ocean tides. These cause changes in fluid pressure and chemical concentration gradients within the coastal aquifer, leading to time varying electrokinetic and exclusion-diffusion potentials. Borehole-referenced SP measurements could be used to characterize and monitor tidal processes in coastal aquifers such as the intrusion of seawater.

1. Introduction

Coastal aquifers are an important water resource but are threatened by the intrusion of seawater. Reduced recharge and/or groundwater abstraction decreases freshwater hydraulic head and can cause the movement of a saline front toward abstraction boreholes [*van Weert et al*., 2009]. The recovery of the aquifer in the area adjacent to a contaminated borehole can take considerable time [*Zhou et al*., 2005]. Geophysical monitoring may assist in avoiding contamination of coastal water supplies.

The most common method for monitoring seawater intrusion is borehole measurements of fluid electrical conductivity (FEC) [*Food* and *Agricultural Organisation*, 1997; *Werner et al*., 2009]. However, FEC monitoring does not facilitate proactive management of abstraction. Active geophysical methods, including electrical resistivity tomography (ERT) and time domain electromagnetic methods (TDEM), can offer a means of remotely detecting the saline front. However, ERT commonly relies on surface monitoring and it can be logistically difficult to lay out long-term surface electrode arrays in densely populated areas. Furthermore, and despite recent advances in such techniques [*de Franco et al*., 2009; *Falgàs et al*., 2009; *Rosas-Carbajal et al*., 2013], ERT and TDEM provide information only about the saturated rock resistivity rather than directly about fluid dynamics within the aquifer.

An alternative, passive geophysical method is self-potential (SP) monitoring. SP arises in order to maintain electrical neutrality when a separation of charge occurs due to gradients in pressure (electrokinetic potential) and/or concentration (exclusion-diffusion potential) [*Revil*, 1999; *Maineult et al*., 2004]. In coastal aquifers, tides alter the pressure and concentration gradients [*Kuan et al*., 2012] and are expected to give rise to SP signals with a tidal signature. An electrokinetic response to pumping has previously been detected in the UK Chalk aquifer [*Jackson et al*., 2012a]. Furthermore, modeling suggests that SP may indicate the movement of a saline front some distance from a monitoring borehole [*Gulamali et al*., 2011; *Bolève et al*., 2011; *Jackson et al*., 2012b; *Jougnot et al*., 2015]. Thus, SP could be used to monitor, remotely, seawater intrusion in real time using a permanent array of borehole electrodes with a reference electrode placed at the surface or within the monitoring borehole.

However, a significant challenge for SP monitoring in coastal aquifers is that the signals of interest, i.e., changes in concentration and pressure gradients induced by ocean tides, may coincide with diurnal and semidiurnal SP fluctuations caused by other sources such as telluric currents, Earth and atmospheric tides, and changes in temperature (Table 1). A number of studies have examined SP responses to induced periodic

Table 1. The Main Periodic Components of the Tides in the English Channel[a]

Period (h)	Cycles per Day (cpd)	Notation	Tidal Mechanism	Amplitude Relative to M_2	Possible Nonoceanic Sources
			Diurnal		
23.934	1.003	K_1	Principal lunar-solar	0.5842	Earth tides
24.066	0.997	S_1	Principal solar	0.1933	Earth tides/telluric/temperature/atmospheric tides
25.819	0.929	O_1	Principal lunar	0.4148	Earth tides/atmospheric tides
26.868	0.893	Q_1	Elliptic lunar	0.0795	Earth tides
			Semidiurnal		
11.967	2.005	K_2	Lunar-solar	0.1267	Earth tides
12.000	2.000	S_2	Principal solar	0.4656	Earth tides/telluric/temperature/atmospheric tides
12.421	1.932	M_2	Principal lunar	1.0000	Earth tides/atmospheric tides
12.658	1.896	N_2	Lunar elliptic	0.1915	Earth tides
			Short Period		
6.301	3.809	MN_4	Shallow water components	0.0297	NA
6.209	3.865	M_4	found in the English Channel	0.1000	NA
6.101	3.934	MS_4		0.0553	NA
			Long Period		
13.661 days	0.070	M_f	Fortnightly	0.1722	Earth tides
			Nonoceanic Components		
8.000	3.000	M_3	Principal solar	NA	Telluric/temperature
6.000	4.000	M_4			

[a]Adapted from *Doodson* [1921], *Apel* [1987], *Hamilton* [1978], *Walters* [1987], and *Baptista et al.* [1989]. Also shown are nonoceanic processes which may contribute to a tidal power spectrum in SP data. NA, not applicable.

processes, including harmonic pumping tests [*Maineult et al.*, 2008; *Revil et al.*, 2008] and drainage-imbibition cycles [*Allègre et al.*, 2014], but few have examined the SP response to natural periodic processes. Diurnal or semidiurnal SP signals have been observed with source mechanisms other than ocean tides, including diurnal spring discharge [*Perrier et al.*, 1999] and flow under glaciers driven by Earth and atmospheric tides [*Kulessa*, 2003]. *Perrier et al.* [1997] and *Bumpus and Kruse* [2014] attributed diurnal SP signals to evapotranspiration causing vertical flow within the unsaturated zone. Other studies attribute the presence of diurnal and semidiurnal SP signals to telluric currents caused by the geomagnetic field [*Perrier et al.*, 1998; *Trique et al.*, 2002].

The few studies that report SP measurements at coastal sites have obtained data using only surface electrode arrays. *Gokhberg et al.* [2009] observed a tidal power spectrum in SP data obtained using 2 km long cables in coastal Japan. They were unable to explain the magnitude of the observed SP solely by invoking Earth tides and suggested that ocean tides contributed. *Kang et al.* [2014] monitored SP at a coastal sea dyke. They observed a semidiurnal SP signal, which they attributed to changes in pressure gradients across the tide, but they did not use frequency analysis to assess the SP data. Furthermore, they used a 6 h sampling rate so aliasing will have occurred and installed steel electrodes, which are unstable and of inadequate quality for SP monitoring [*Perrier et al.*, 1997]. If changes in salinity occurred at their electrodes as seawater moved through the dyke, then redox potentials will have arisen [*Castermant et al.*, 2008]. Both *Gokhberg et al.* [2009] and *Kang et al.* [2014] neglected the impact of the geomagnetic ocean dynamo, and *Kang et al.* [2014] neglected Earth tides, yet these processes may have led to the SP responses they observed.

The aim of this study was to establish whether SP responds to changes in pressure and concentration gradients in a coastal aquifer driven by ocean tidal processes. The objectives were to (i) measure SP in the UK Chalk aquifer, (ii) assess the contribution of various tidal processes by comparing inland and coastal, and surface- and borehole-referenced SP data, and (iii) determine whether ocean tides induce a measureable tidal SP. Table 1 shows the dominant tidal components in the English Channel along with hypothesized SP sources.

2. Method

Two sites in the Upper Chalk aquifer [*Bristow et al.*, 1997] of the UK were used to investigate the source of tidal SP. Figure 1 shows the layout of the surface and borehole arrays at the inland site near Trumpletts Farm in Berkshire and the coastal site at Saltdean in East Sussex.

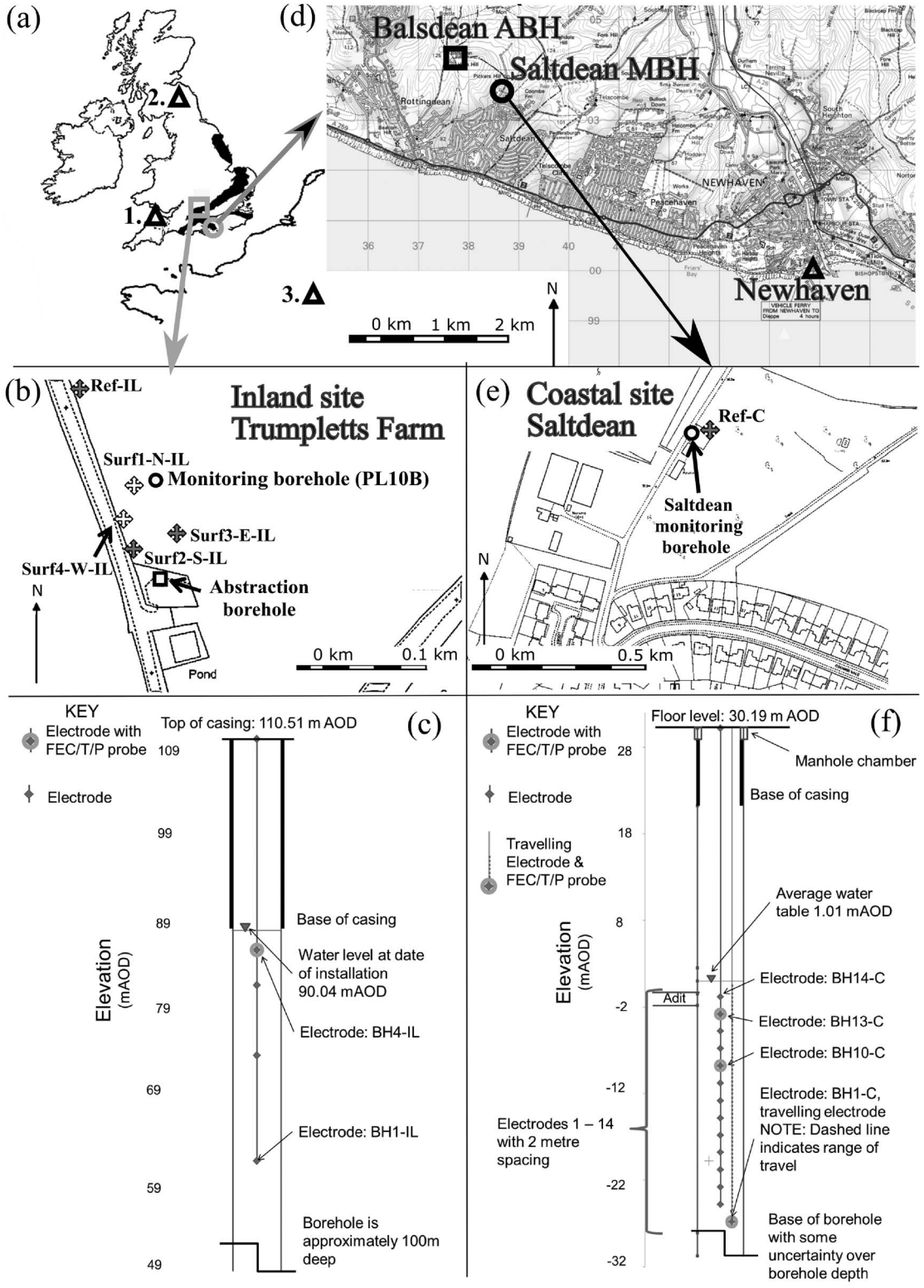

Figure 1. (a) Inland (hollow grey square), coastal (hollow grey circle) SP monitoring sites and geomagnetic stations (hollow triangles). The Chalk aquifer is shaded black. (b) Inland site showing surface electrodes (crosses) and abstraction and monitoring boreholes (hollow square and circle). Temperature was measured at electrodes shaded grey. The inland site is rural but adjacent to two minor roads (shown as solid lines). (c) Inland borehole array. (d) Coastal site showing monitoring borehole (MBH, hollow circle), abstraction borehole (ABH, hollow square) and tidal gauge (hollow triangle). (e) Closeup of coastal site showing the monitoring borehole (hollow circle) and surface reference electrode (grey cross), where temperature was also measured. The coastal site is semiurban with buildings and roads shown as solid lines. (f) Coastal borehole array. Maps: © Crown copyright and database rights 2015 Ordnance Survey (Digimap License).

2.1. Site Descriptions

The inland site has been extensively investigated as part of a research program on lowland catchments [*Williams et al*., 2006; *Wheater et al*., 2007; *Mathias et al*., 2007; *Butler et al*., 2009]. The site consists of six 100 m boreholes close to an abstraction borehole which is infrequently used. The boreholes penetrate New Pit Chalk, ~3 m of Chalk Rock and then ~20 m of Lewes Nodular Chalk [*Schürch and Buckley*, 2002; *Woods*, 2006]. The Seaford Chalk formation then extends to the surface. Borehole PL10B was instrumented (Figures 1b and 1c).

The borehole at the coastal site is used to monitor FEC (as a proxy for salinity) seaward of the Balsdean abstraction borehole (Figures 1d–1f). FEC in the borehole can reach 15,000 μS/cm as regular breakthrough of saline water occurs [*Jones and Robins*, 1999]. The borehole penetrates the fine-grained Upper Cretaceous Seaford Chalk and the coarser grained Lewes Nodular Chalk in the lower 12 m of the borehole. Ocean tides are recorded at Newhaven (Figure 1d) [*British Oceanographic Data Centre*, 2015].

2.2. Data Acquisition

At both sites at least one surface reference electrode was available. The shallowest borehole electrode was used as the borehole reference. The borehole arrays comprised nonpolarizing Silvion Ag/AgCl WE300 potable water electrodes [*Silvion*, 2015]. Surface electrodes were Silvion Ag/AgCl WE200 soil electrodes [*Silvion*, 2013]. In both electrode types, the Ag/AgCl rod is housed inside a plastic casing containing KCl gel. The casing is separated from its surroundings by a low permeability ceramic disk. The WE300 electrodes have a 0.05 M internal KCl concentration, and the WE200 electrodes have a 0.5 M internal KCl concentration. Surface temperature was measured using Campbell Scientific 107-L thermistors. AquaTroll 200 FEC/T/P probes were used to measure FEC, temperature (T), and pressure (P) in the borehole and were placed next to selected electrodes (Figures 1c and 1f). At both sites, data were logged at a 5 min time interval with a Campbell Scientific CR3000 data logger. This device has a 20 GΩ internal impedance, a resolution of 0.67 μV, and an accuracy of 0.04%. The electrodes were connected to the logger using 5 mm diameter coaxial cable. Data at the coastal site were collected from May 2013 to January 2015 and at the inland site from May 2015 to August 2015, although not all data types were recorded throughout.

At the inland site, four surface monitoring electrodes were installed around the monitoring borehole (Figure 1b) and were referenced against a surface electrode 90 m north of the monitoring borehole. The electrodes were installed at a depth of ~0.5 m, in a bucket filled with saturated bentonite, ensuring a good electrical connection with the ground [*Corwin*, 1990; *Perrier et al*., 1997; *Trique et al*., 2002]. Temperature was measured at Ref-IL, Surf2-S-IL, and Surf3-E-IL. Four electrodes spaced with respect to the shallowest electrode, at ~24 m, ~12 m, ~8 m, and ~4 m, were installed in the monitoring borehole (Figure 1c). The maximum spacing between electrodes matched the maximum electrode spacing at the coastal site. An FEC/T/P probe was installed at the top of the borehole.

At the coastal site, only a reference electrode was installed at the surface and 14 electrodes spaced at 2 m intervals were installed in the borehole (Figure 1f). Three FEC/T/P probes were installed at the top, middle, and bottom of the water column. The spacing between the shallowest and deepest electrodes was ~24 m. In order to minimize exposure to diurnal and seasonal temperature variations, the surface reference electrode and a thermistor were buried at ~1.5 m in a plastic bucket filled with saturated bentonite (Figure 1e). It was not possible to install a surface array at the coastal site.

2.3. Spectral Analysis Method

A number of different spectral analysis techniques have been used in previous studies to analyze periodic SP signals [*Allègre et al*., 2014; *Kulessa et al*., 2003; *Maineult et al*., 2008]. In this study, the Lomb-Scargle power spectral density (PSD) periodogram [*Lomb*, 1976; *Scargle*, 1982] was used to analyze SP. The Lomb-Scargle PSD, a least squares spectral analysis technique, was chosen because it can be used with time series data that have gaps or that are not evenly spaced in time [*Lomb*, 1976; *Trauth*, 2010]. The Lomb-Scargle PSD offers an alternative approach to dealing with data gaps to that proposed by *Mariethoz et al*. [2015]. It also allowed determination of the probability of a certain frequency peak being related to a real periodic signal and not the result of random fluctuations; i.e., the probability of detection [*Trauth*, 2010]. The significance limits were set at 50, 90, 99 and 99.99% and are shown in all PSD plots using dashed lines. No data smoothing or filtering was conducted prior to spectral analysis.

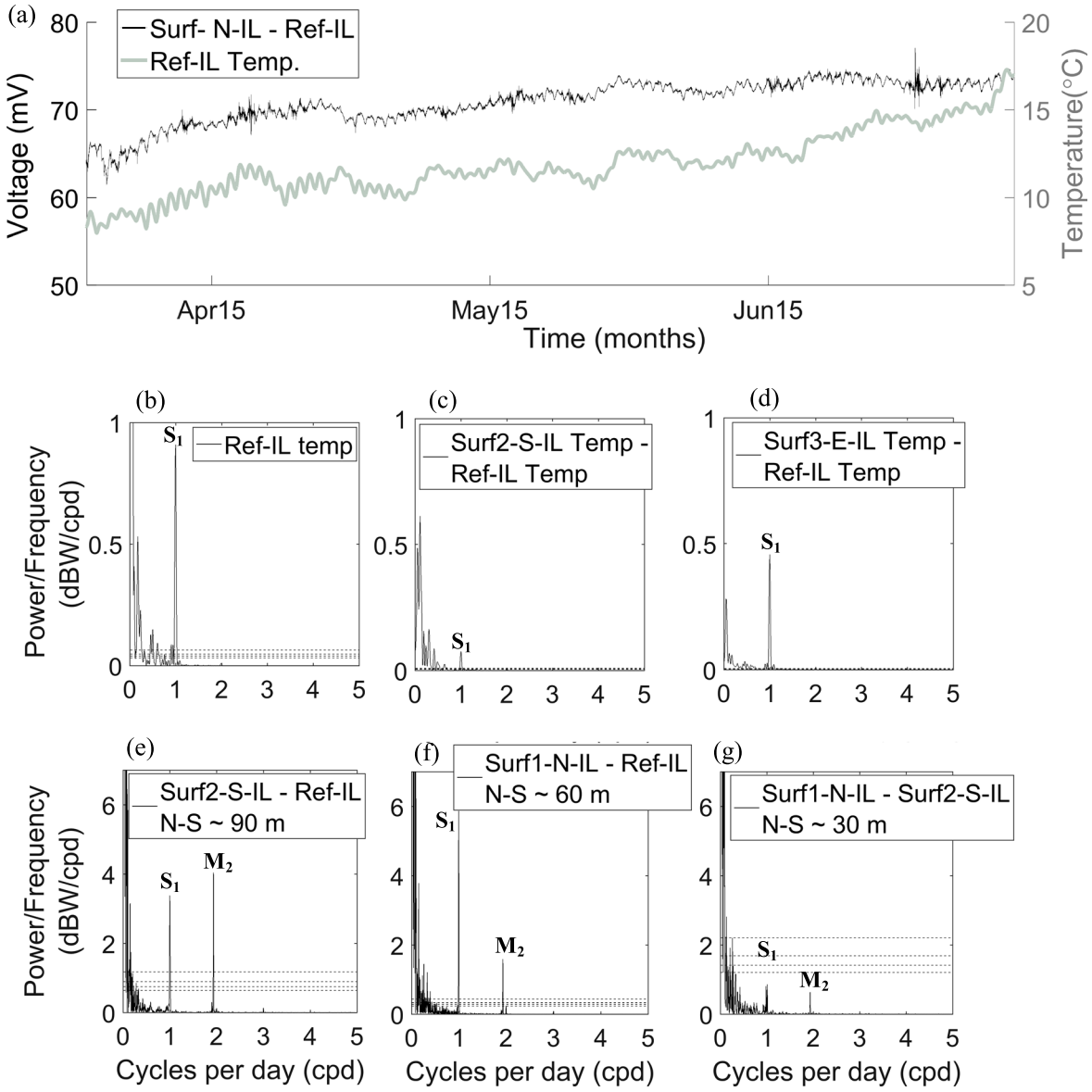

Figure 2. Surface data from the inland site. (a) Typical SP data from the surface array and temperature measured at Ref-IL. (b–d) PSD of temperature data and temperature differences across the surface array. (e–g) PSD of SP data from the N-S dipoles in the array; the dipole spacing is indicated. Note that the east-west dipoles only contained S_1 and are not shown here. The surface data used in the analysis at the inland site did not coincide exactly with the time series used for the borehole data. Reasons for this included equipment failure and environmental factors.

3. Results

3.1. Inland Site

Surface SP data from three north-south dipoles at the inland site are shown in Figures 2e–2g. All dipoles displayed the diurnal principal solar component (S_1). The north-south dipoles also displayed the semidiurnal principal lunar component (M_2). The magnitude of the M_2 component decreased with the length of the dipole. Temperature measured at the electrodes, and temperature differences across the dipoles, also displayed S_1 but did not show any other spectral components (Figures 2b–2d; the raw data are shown in Figure 2a).

In the monitoring borehole at the inland site, the temperature was stable and showed no specific frequency response (Figure 3a) but the head contained the diurnal (S_1) and semidiurnal (S_2) principal solar components, although both were below 50% significance (Figures 3b–3d).

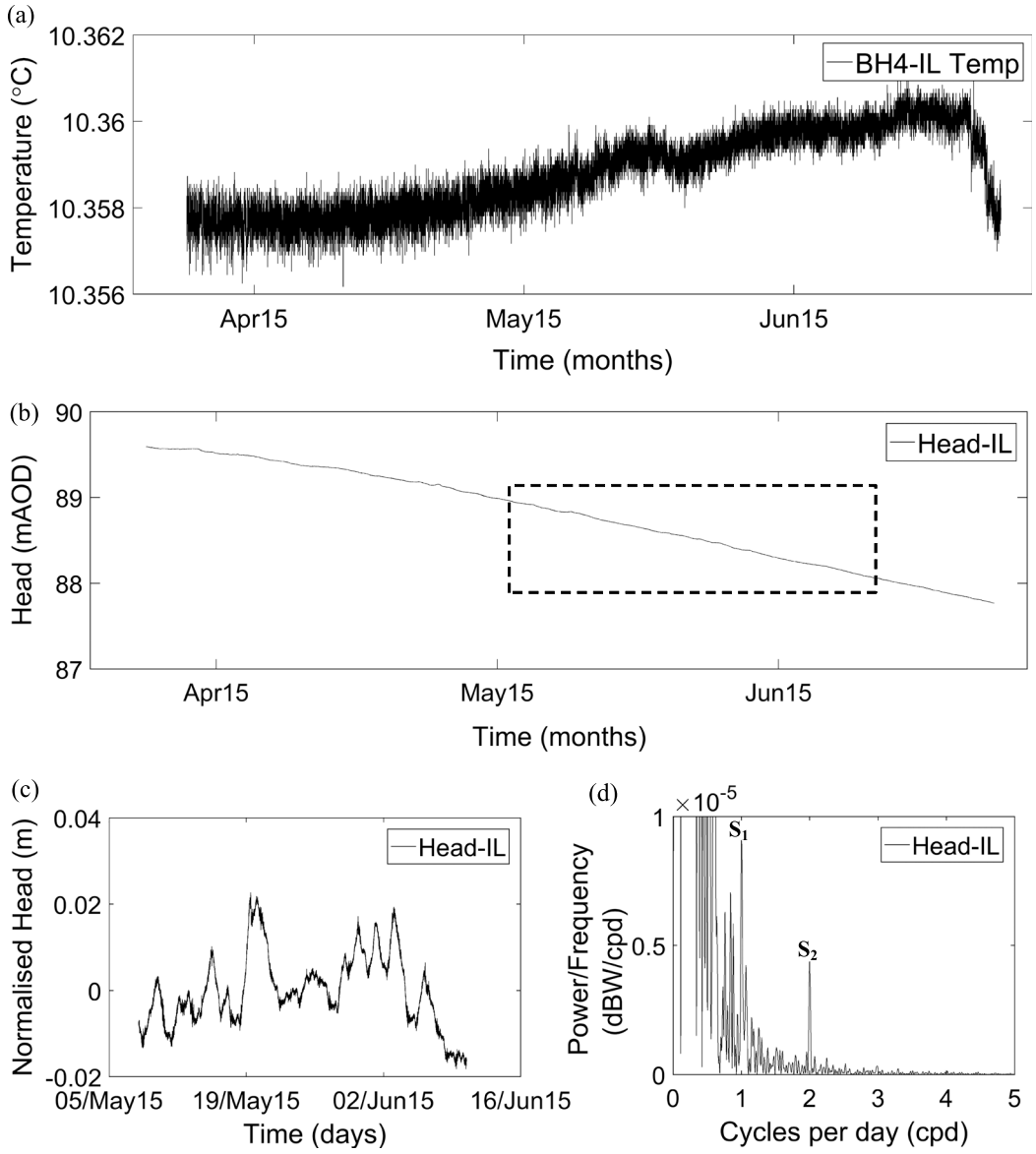

Figure 3. Data from the inland borehole. (a) Temperature in the monitoring borehole. (b) Head in the monitoring borehole, it was necessary to use an optimized subdata set, shown by the dashed box, for the PSD analysis due to the nature of the data. (c) Head, used in the PSD analysis, detrended by removing the best straight line fit. (d) PSD of the head (below 50% significance).

Figure 4 shows the PSD of the SP recorded at the deepest borehole electrode, referenced sequentially against different electrodes in the surface array. All dipoles displayed S_1 and M_2 and, as the distance of the reference electrode from the borehole increased, the M_2 component also increased.

In contrast to the surface-referenced borehole data, there were no significant periodic components recorded in the borehole electrodes when referenced against the shallowest borehole electrode (BH4-IL) (Figure 5). The origin of the long-term trend observed in Figure 5a is unclear. Each of the other borehole electrodes (not shown) displayed a slightly different onset and nature of trend, suggesting an electrode artifact. However, further analysis of the trend is beyond the scope of this paper (see *Jackson et al.* [2012a] for further discussion of SP monitoring at the inland site).

3.2. Coastal Site

In order to compare the PSD analyses from the inland and coastal sites it was necessary to use a similar time series length of ~3 months. Comparing 1.5 years of data from the coastal site (Appendix A) with

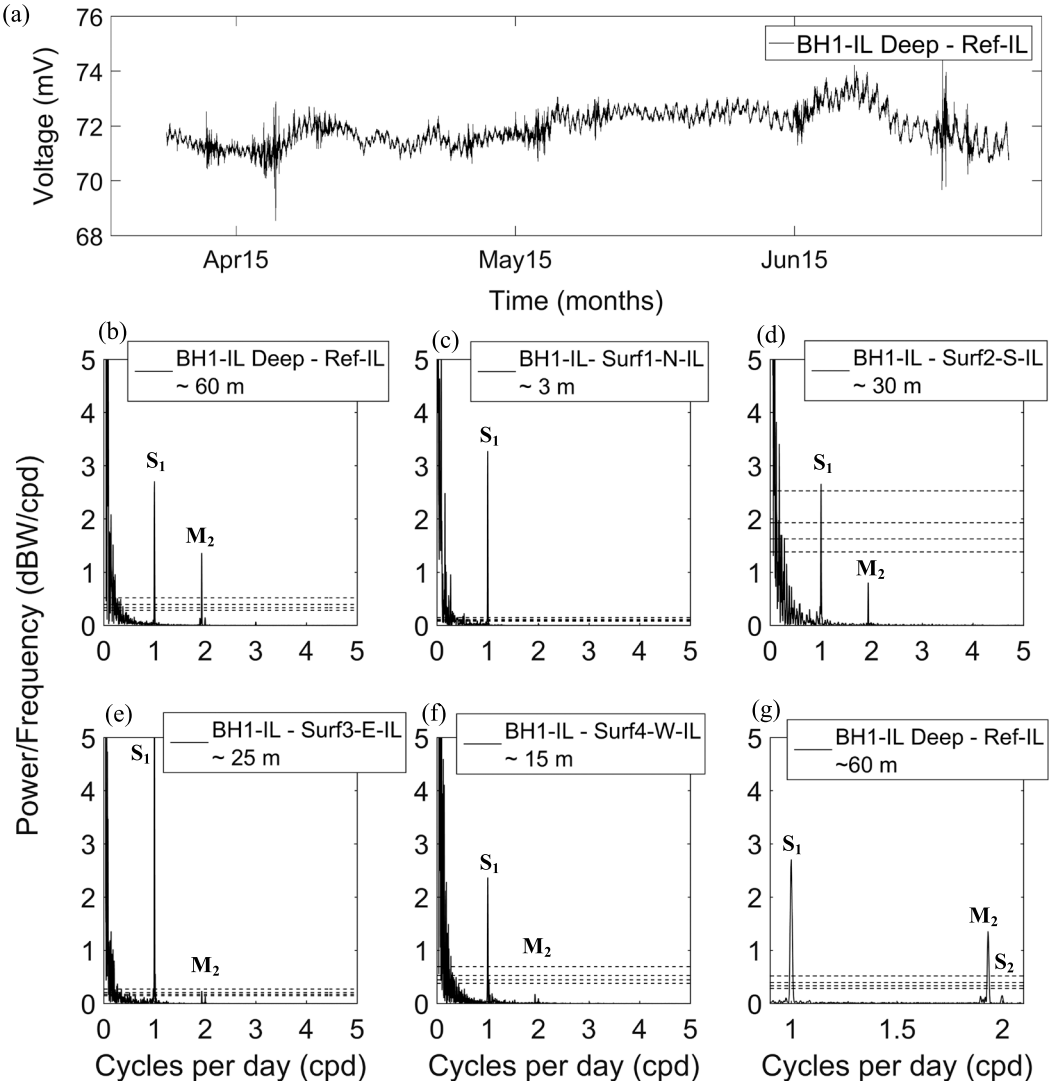

Figure 4. Borehole data from the inland site. (a) Surface-referenced SP at the deepest borehole electrode. (b–f) PSD of the SP at the deepest borehole electrode referenced against different surface electrodes (approximate lateral electrode spacing is indicated). (g) Closeup of Figure 4b focusing on diurnal and semidiurnal periods.

3 months of data from the inland site would have produced a bias in favor of the coastal site [*Karl*, 1989; *Trauth*, 2010]. It was not possible to gather a longer time series from the inland site. Data from the coastal site collected from May to August 2013 were analyzed, which corresponds to the same time of year as the inland data acquisition providing confidence in the comparison of the data sets. It was not possible to collect simultaneous data sets.

Figure 6 shows the results of PSD analysis for the tidal gauge data at Newhaven. Data from the shorter time period are shown; the full data are presented in Appendix A. The main frequency components identified in the PSD of the data from the shorter time period are the same as those identified over the long time period for all data types (tidal gauge, borehole head, temperature, conductivity, and SP). The tidal gauge data were dominated by the diurnal principal lunar component (M_2). There was also evidence of S_2 and N_2 and an indication of K_1, MN_4, M_4, and MS_4 (Figures 6b–6d and Appendix A).

Head fluctuations measured in the borehole at the coastal site contained the main tidal components M_2, K_1, S_2, and N_2, similar to the tidal gauge data (Figures 7a and 7b). The borehole FEC and temperature data were dominated by the M_2 component (Figures 7c–7f). FEC increased slightly in mid-August 2013 due to decreased head. There were no significant temperature fluctuations at the surface electrode (Figures 7g–7h).

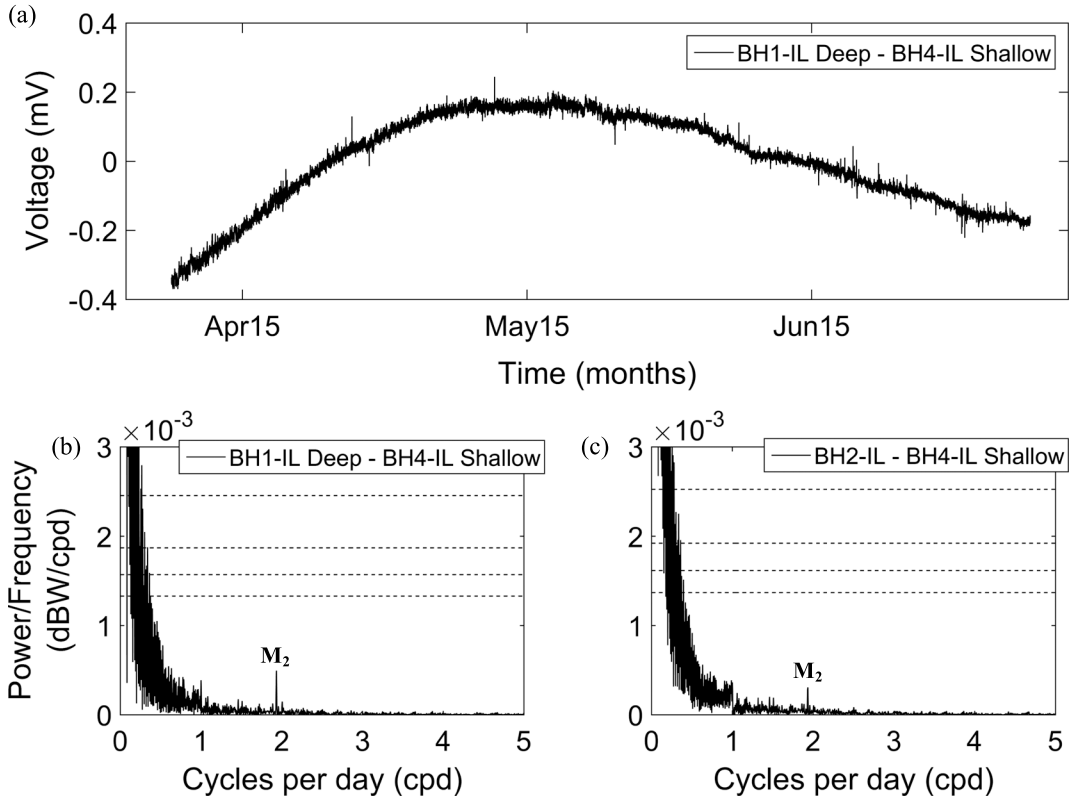

Figure 5. Borehole data from the inland site. (a) SP data from the deepest electrode referenced against the shallowest borehole electrode. (b–c) PSD of borehole-referenced SP for two different dipoles.

Surface-referenced borehole SP data were dominated by the M_2 component, but K_1, S_2, and N_2 components were also present (Figure 8), similar to the tidal gauge and borehole head data. It is notable that the M_2 component in surface-referenced borehole SP data at the coastal site was an order of magnitude larger than in comparable data at the inland site (Figure 4f). There was also an indication of S_3, MN_4, M_4, MS_4, and S_4 (Appendix A).

Borehole-referenced SP was dominated by the M_2 component, although a small K_1 component was also present (Figure 9). The magnitude of the M_2 and K_1 responses increased as the separation of the electrodes increased. The smallest separation at which M_2 appeared was ~8 m (Figure 9h). It is again notable that these data show a strong M_2 component, unlike the comparable data at the inland site (Figure 5).

4. Discussion

Table 2 shows a summary of the periodic components in the SP data at both sites and the hypothesized source mechanisms. The components in borehole-referenced SP at the coastal site almost exactly match those of ocean tides. Furthermore, for the reasons outlined below, the absence of significant periodic tidal components in the borehole-referenced SP at the inland site suggests that Earth, atmospheric or geomagnetic tides, are not primarily responsible for the tidal SP response observed at the coastal site. Figure 10 shows the M_2 component for surface and borehole-referenced SP at both sites for two dipoles of comparable length. The M_2 component was orders of magnitude larger in the coastal SP data, suggesting that distinct SP sources are present in the coastal aquifer and are driven by ocean tides. However, because the M_2 component was present in surface-referenced SP data at the inland site, caution was required before attributing the M_2 response at the coastal site to ocean tides. We discuss the various possible sources of the observed SP response at each site in more detail in the following sections.

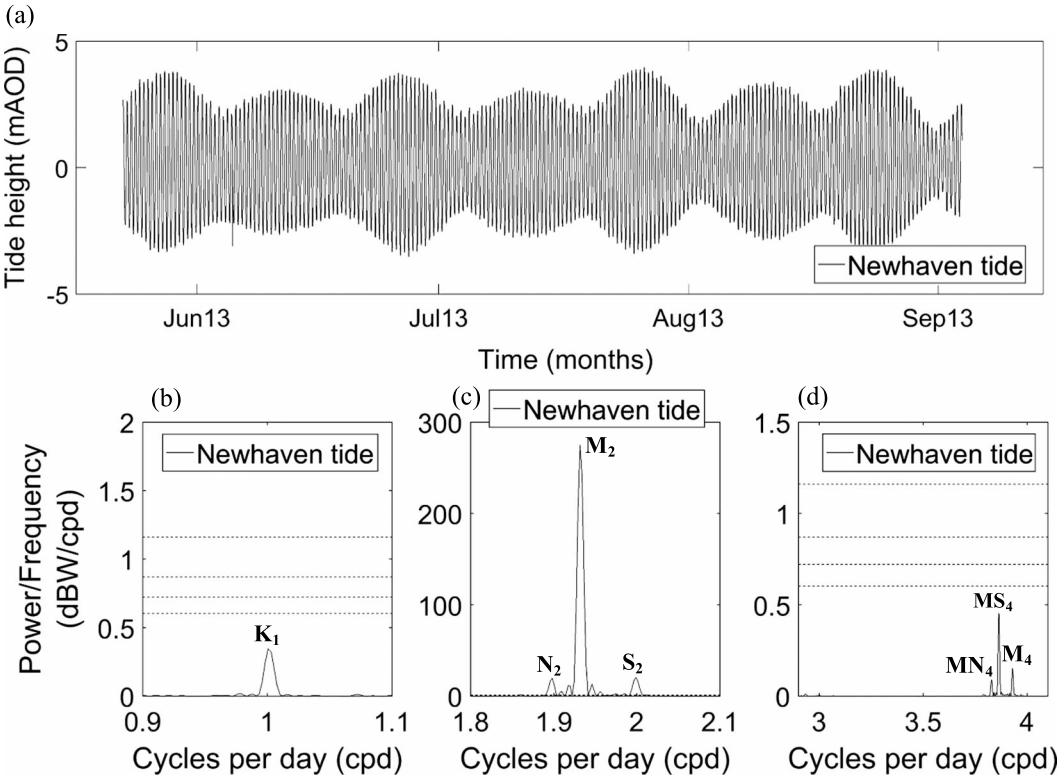

Figure 6. Data from the coastal site. (a) Tidal gauge data from Newhaven; (b) diurnal, (c) semidiurnal, and (d) short period tides.

4.1. Temperature and Conductivity

At the inland site, the surface-referenced SP data showed a significant S_1 component (Figures 2 and 4), similar to the temperature data at the surface electrodes (Figures 2b–2d). Temperature fluctuations at, and between, the surface electrodes, and the temperature sensitivity of the electrodes, likely contributed to the S_1 response in the surface-referenced SP data. Differences in temperature fluctuations between electrode locations (Figures 2c–2d) explain the differing magnitude of S_1 across the site (Figures 2e–2g). The electrodes have a reported temperature coefficient of −0.65 mV/°C [*Silvion*, 2015]. However, at the coastal site, the surface reference electrode was buried at 1.5 m, below the penetration depth of diurnal temperature fluctuations (Figure 7g) [*Perrier et al.*, 1997]. Temperature fluctuations in both the inland and coastal boreholes were small, which partly explains why there was no S_1 component in SP data from the coastal site, or in borehole-referenced SP data at either site (Table 2).

Borehole FEC data at the inland site showed no detectable frequency response. However, at the coastal site, both temperature and FEC fluctuated with a predominantly M_2 component, although a K_1 component was also present, most clearly in the temperature data (Figures 7d and 7f). Thus, the borehole temperature and FEC share the same key frequency components as the borehole SP data at the coastal site. However, the magnitudes of the fluctuations in temperature and FEC (~0.08°C and 50 μS/cm, respectively) are too small to be responsible for the SP response. The temperature fluctuations yield a maximum temperature contribution of 52 μV for the electrode sensitivity reported above, which is an order of magnitude less than the observed fluctuation of ~600 μV in the SP data (Figure 12a).

Figure 12c shows a crossplot of borehole FEC versus SP and clearly illustrates that there is no direct relationship. Furthermore, the SP fluctuations do not correspond to the FEC fluctuations (Figure 12(b)); moreover, when the FEC increased in late July 2013, there was no corresponding change in SP (compare Figure 7e and Figures 8a and 9a). Thus, SP was not directly caused by the FEC fluctuations observed in the borehole.

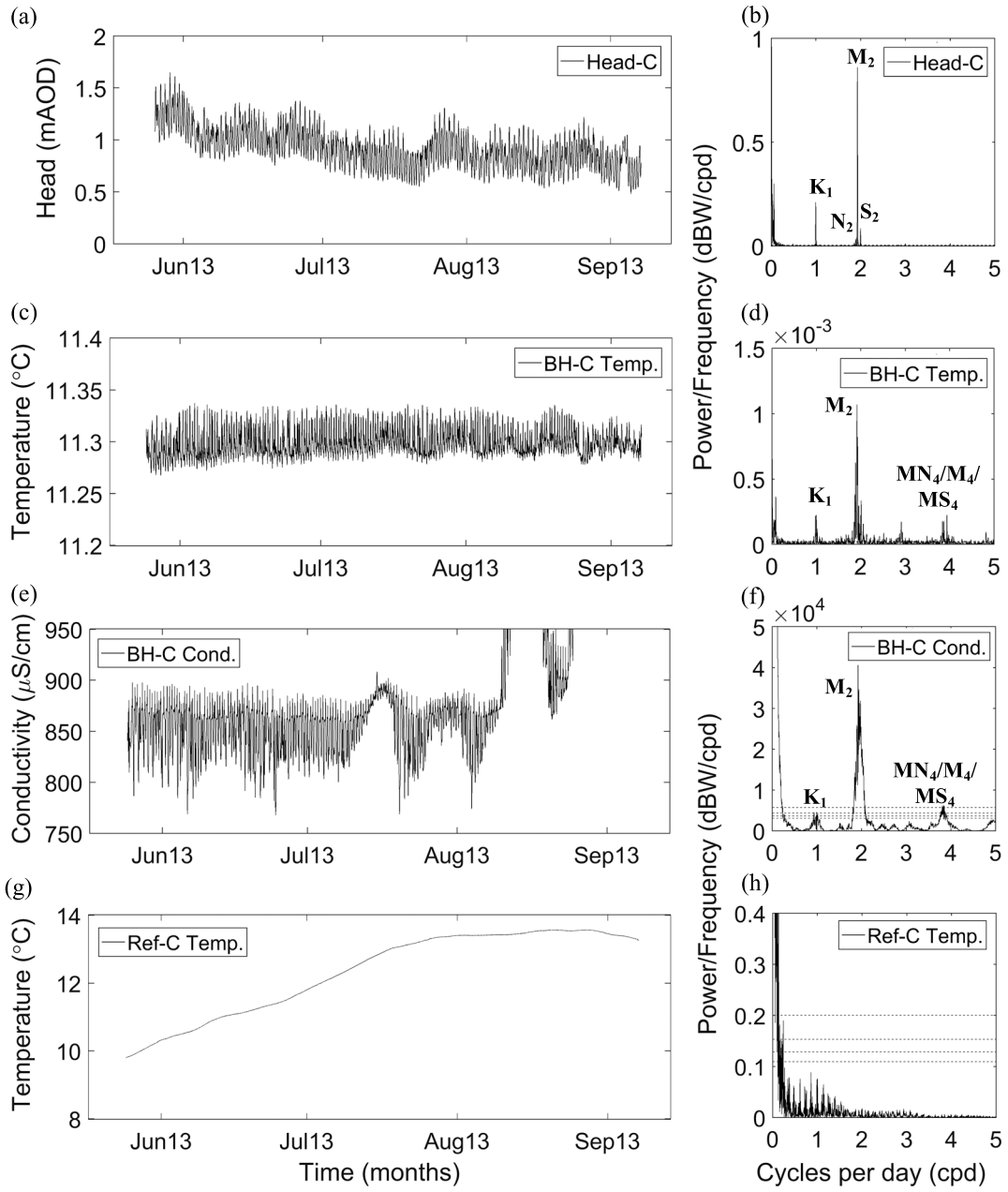

Figure 7. Data from the coastal site. (a) Borehole head. (b) PSD of head. (c) Borehole temperature. (d) PSD of temperature. (e) Borehole FEC; note that at the end of August 2013, saline water entered the borehole and the FEC increased beyond the chosen axis scale. (f) PSD of FEC. (g) Surface temperature (at reference electrode). (h) PSD of surface temperature.

4.2. Geomagnetism

Trique et al. [2002] interpreted the M_2 component in SP data obtained from a surface electrode array in the Alps as ocean tidal modulation of the geomagnetic field. The observation of M_2 in the geomagnetic field is a global phenomenon [*Cochrane and Srivastava*, 1974; *Lilley and Parker*, 1976; *Cueto et al.*, 2003; *Maus and Kuvshinov*, 2004; *Love and Rigler*, 2014]. The movement of ocean water through the geomagnetic field induces an electric current [*Kendall and Chapman*, 1970; *Hewson-Browne*, 1973], a phenomenon known as the ocean dynamo [*Rosser and Schlapp*, 1990; *Palshin et al.*, 1996]. The ocean dynamo is known to generate telluric currents in the UK [*Chapman and Kendall*, 1970; *Osgood et al.*, 1970; *Brown and Woods*, 1971; *Hart*

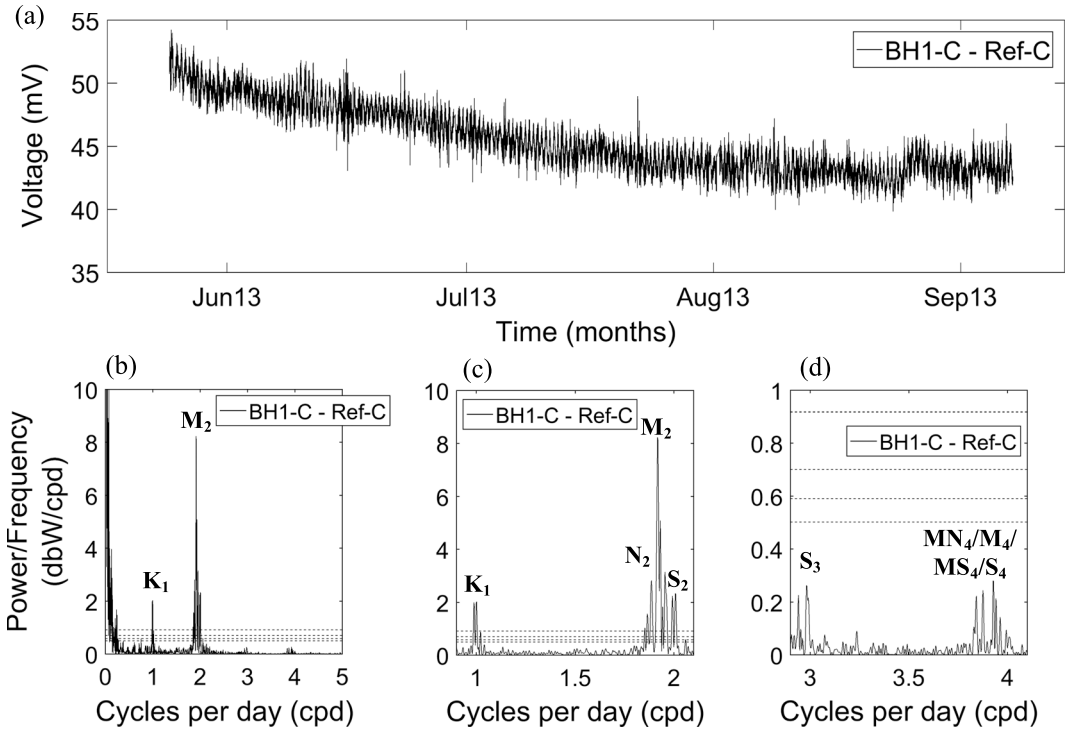

Figure 8. Data from the coastal site. (a) Surface-referenced borehole SP at the deepest electrode (BH1-C). (b) PSD analysis of the surface-referenced borehole SP at BH1-C. (c) PSD of BH1-C in Figure 8b zoomed on diurnal and semidiurnal periods. (d) PSD of BH1-C in Figure 8b zoomed on shorter period components.

et al., 1983b; *Hart et al*., 1983a]. The strength of the telluric contribution to measured SP depends on the length and orientation of the electrode dipoles [*Orihara et al*., 2012]. Thus, the presence of the M_2 component in surface-referenced SP at both sites (Figures 2, 4, and 8) suggests that geomagnetism could have contributed (Table 2). Figure 11 shows the PSD of the geomagnetic field declination and horizontal and vertical intensity from three stations around the SP monitoring sites (Figure 1a).

The geomagnetic field is dominated by the principal solar component (S_1) and contains S_2, S_3, and S_4 harmonics. The presence of S_3 and S_4 in the long time series surface-referenced SP at the coastal site (Appendix A) provides an indication of geomagnetic influence, because S_3 and S_4 can only be explained by telluric currents.

The relative magnitude of each component at the three geomagnetic stations was approximately the same (Figure 11). Most significantly, the M_2 component was consistently smaller than S_1 and S_2. Globally, the S_2 component of the geomagnetic field is larger or comparable to M_2 [*Cochrane and Srivastava*, 1974; *Maus and Kuvshinov*, 2004; *Love and Rigler*, 2014; *Bindoff et al*., 1988]. If the geomagnetic field were dominantly responsible for the SP fluctuations at both sites, then the SP data would be expected to show a similar power spectrum to the geomagnetic data. This is not the case, although the relationship between dipole length and SP response at the inland site (Figure 2) indicates that the geomagnetic field does contribute to the S_1 and M_2 components observed in surface SP data, as suggested by *Trique et al.* [2002].

Borehole-referenced SP data at both sites showed no S_1 component (Figures 5 and 9), and only the coastal site showed a significant M_2 component (Figure 9). Thus, the geomagnetic field did not make a significant contribution to the large M_2 component observed in the SP data at the coastal site.

4.3. Earth and Atmospheric Tides

There was some indication of the principal solar component (S_1) and its harmonic (S_2) in the head fluctuations at the inland borehole (Figure 3d). Such head fluctuations are most likely caused by atmospheric pressure, which fluctuates with S_1 and S_2 period [*Dai and Wang*, 1999]. *Rojstaczer and Riley* [1990] and *Kumpel* [1997]

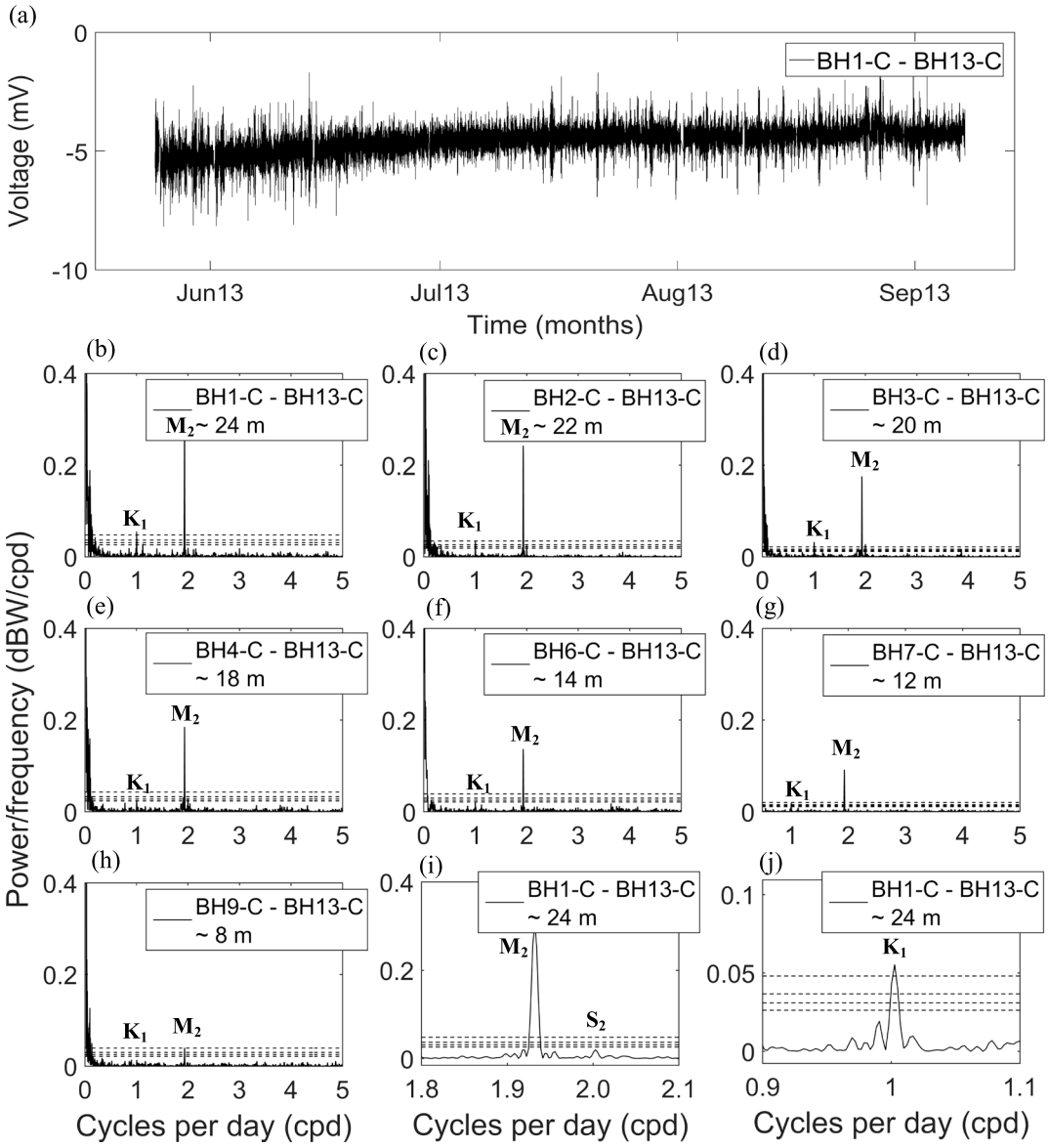

Figure 9. Data from the coastal site. (a) Borehole-referenced SP at the deepest electrode (BH1-C). (b–h) PSD of SP data from dipoles with decreasing separation from BH13-C (top of borehole). The length of dipole is indicated in each plot. (i) PSD of BH1-C in Figure 9b zoomed on semidiurnal periods. (j) BH1-C in Figure 9b zoomed on diurnal periods.

showed that diurnal (O_1, S_1) and semidiurnal (M_2, S_2) water level fluctuations in boreholes can be caused by atmospheric and Earth tides and can occur in confined and unconfined aquifers (Table 2). Thus, Earth and atmospheric tides can cause groundwater flow and electrokinetic potentials, via periodic compression and release of the Earth's crust.

Earth tides share the same relative amplitude for each of the periodic components as ocean tides [*Agnew*, 2007]; thus, they may contribute to the M_2 component observed in borehole or surface-referenced SP. *Kulessa et al.* [2003] invoked Earth tides as the primary driving mechanism for subglacial flow leading to a significant K_1 component in their SP. *Gokhberg et al.* [2009] modeled observations of tidal SP on kilometer long surface cables in Japan and attributed the presence of the main tidal components (O_1, P_1, K_1, N_2, M_2, and S_2) to the electrokinetic potential caused by Earth tides. However, assuming that Earth tides are of the same order of magnitude at the inland and coastal sites [*Agnew*, 2007], then Earth tide effects are too small to explain the SP components at the coastal site, primarily because of the absence of any significant M_2 component within the inland borehole-referenced SP (Figures 5 and 10).

Table 2. Summary of the Periodic Components in the SP Data and Hypothesized Source Mechanisms[a]

Data Set	Semidiurnal			Diurnal			Largest Periodic Component	Hypothesized Primary SP Sources
	M_2	S_2	N_2	K_1	O_1	S_1		
SP Data								
Coastal BH surface reference	**3**	1	2	2	2	0	M_2	Oceanic tide (EED/EK)
Coastal BH referenced	**3**	2	1	2	2	0	M_2	Oceanic tide (EED/EK)
Inland surface array	2	1	0	0	0	3	S_1	Temperature (electrode)
Inland BH surface referenced	2	1	0	0	0	3	S_1	Temperature (electrode)
Inland BH referenced	0	0	0	0	0	0	NA	NA
Possible SP Source Mechanisms								
Oceanic tide	**3**	2	1	2	1	0	M_2	
Geomagnetic field	1	2	0	0	0	3	S_1	
Temperature	0	1	0	0	0	3	S_1	
Earth tide[b]	**3**	2	1	2	1	0	M_2	
Atmospheric tide[b]	0	3	0	0	0	1	S_2	

[a]Dark grey shading indicates borehole-referenced SP. Light grey shading highlights surface-referenced SP. Periodic magnitudes are ranked: 3—largest, 2—intermediate, 1—smallest, 0—below 50% significance. NA, not applicable.
[b]Earth tides were estimated from *Agnew* [2007] and atmospheric tides from *Lindzen and Chapman* [1969] and *Dai and Wang* [1999].

SP processes in the unsaturated zone have been investigated by previous authors, who found that the source mechanisms are nontrivial. For example, *Maineult et al*. [2008] and *Revil et al*. [2008] found that SP measured during harmonic pumping tests and referenced using an electrode in the unsaturated zone produced nonlinear responses to the periodic change in pressure induced by the pumping tests. *Maineult et al*. [2008] attribute these nonlinear effects to saturation and desaturation processes occurring in the unsaturated zone. Unsaturated zone processes are briefly discussed here because they may also explain why M_2 was observed in surface-referenced data at both sites. *Adler et al*. [1997] attributed SP fluctuations, from a few hours to

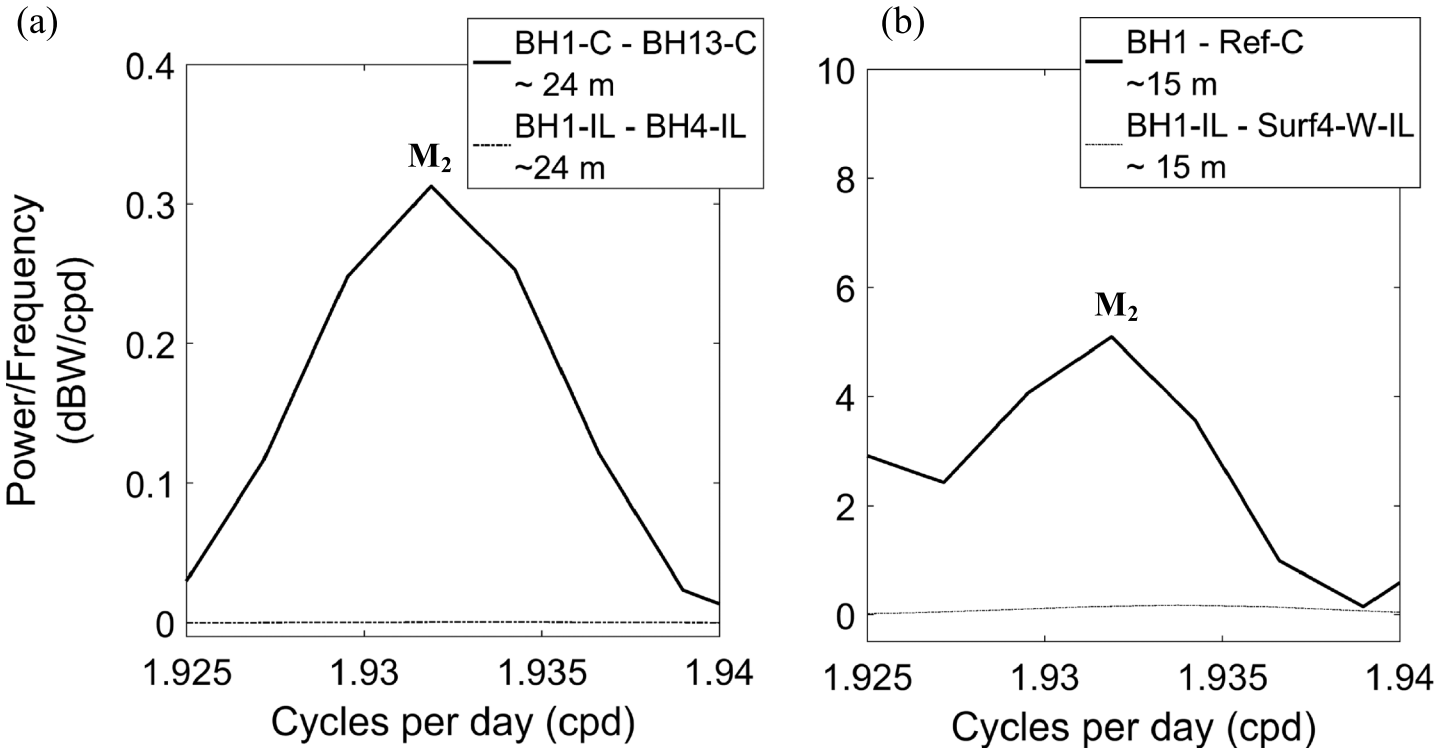

Figure 10. PSD focussing on the M_2 components of the SP at coastal and inland sites for comparable dipole lengths in (a) borehole-referenced data and (b) surface-referenced data. Dipole lengths are shown.

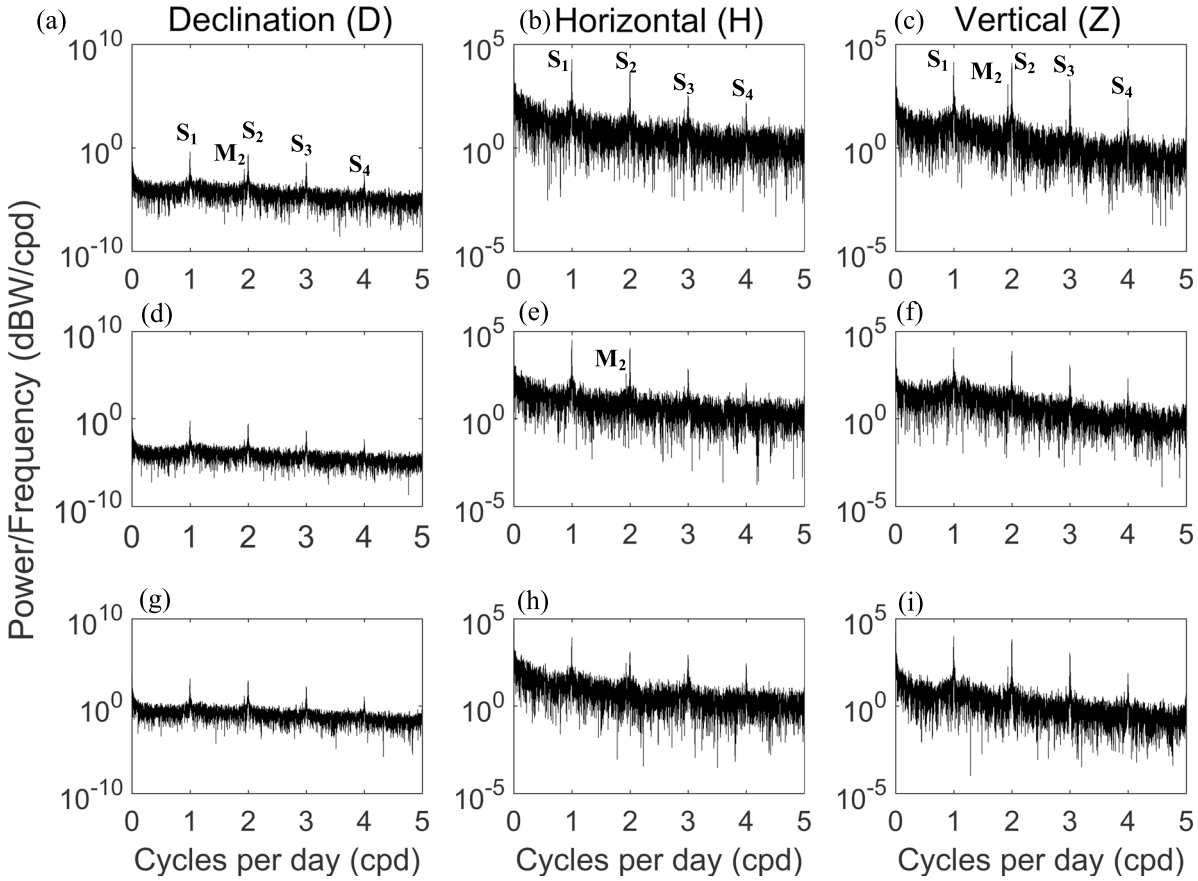

Figure 11. Geomagnetic PSD for the duration of the inland monitoring experiment from (a–c) Hartland, UK, (d–f) Eskdalemuir, UK, (g–i) Chambon-la-Foret, France, location 1., 2. and 3. in Figure 1a respectively.

1 day, to periodic variations in saturation driven by atmospheric fluctuations. The M_2 component is a constituent of atmospheric tides [*Geller*, 1970; *Vial and Forbes*, 1994; *Forbes et al*., 1994], albeit not as prominent as S_1 or S_2 [*Lindzen and Chapman*, 1969]. *Kulessa et al*. [2003] invoked atmospheric tides to explain the S_2 component in their SP, suggesting that semidiurnal atmospheric fluctuations contributed to subglacial flow. Earth or atmospheric tides may not generate any significant change in pressure gradients within the aquifer but may drive flow or changes in saturation, within the unsaturated zone and in turn generate a measureable electrokinetic potential at electrodes installed at, or close to, the surface [*Linde et al*., 2011; *Jougnot et al*., 2012; *Allègre et al*., 2014]. Thus, Earth and/or atmospheric tides may explain the M_2 signal recorded in our surface-referenced data. It is clear that surface SP monitoring is fraught with interpretation difficulties, including multiple overlapping source mechanisms.

4.4. Ocean Tides

The borehole-referenced SP data at the inland site contained no significant frequency components. In contrast, the borehole-referenced SP data at the coastal site contained significant M_2 and K_1 components, consistent with the borehole head and tidal gauge data. The above analysis, by ruling out alternative processes, suggests that these tidal components in the coastal borehole SP data must be caused by changes in pressure and/or concentration gradients (i.e., the electrokinetic (EK) or exclusion-diffusion (EED) potential) in the aquifer, driven by tides in the English Channel. Figure 12 shows coastal SP, head, and conductivity in July and August 2013. The SP, here smoothed with a 2 h window, is anticorrelated with head, which is consistent with a negative EK coupling coefficient as measured in chalk [*Jackson et al*., 2012a].

The head fluctuations observed in the coastal borehole are ~0.5 m (Figure 12a), and the maximum EK contribution is estimated using the coupling coefficient (-0.575 ± 0.080 mV/mH_2O in *Jackson et al*. [2012a]) resulting in a ~290 μV EK contribution, around half the ~600 μV fluctuation observed in the borehole-

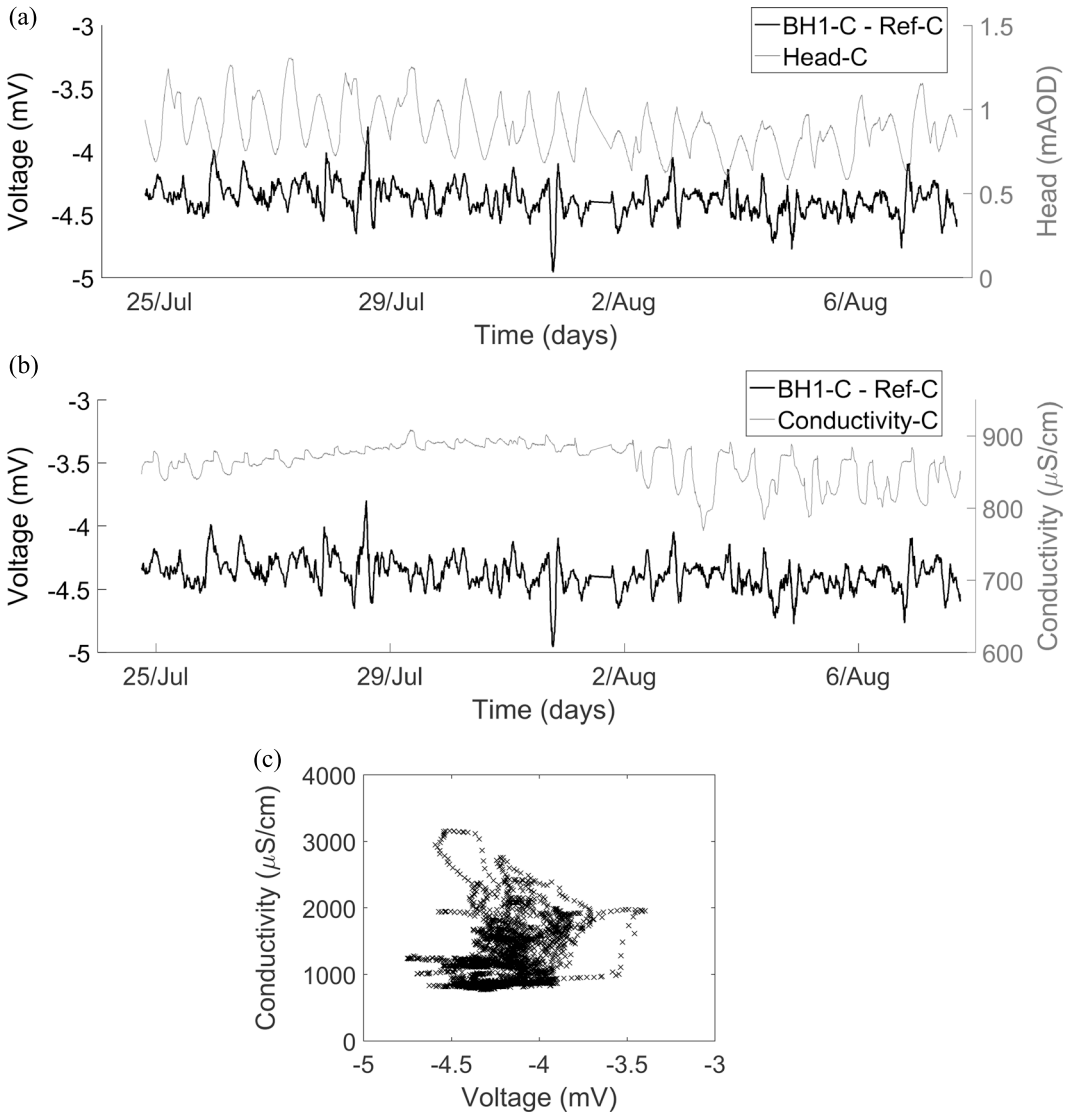

Figure 12. Borehole-referenced data from the coastal site. (a) Head and SP. (b) FEC and SP. (c) Crossplot of FEC and SP.

referenced SP data. This estimate is consistent with observations made by *Jackson et al*. [2012a] who measured a ~60 μV response to a ~0.1 m drawdown during pumping of the abstraction borehole at the inland site (Figure 1b). Thus, it appears that the EED potential, caused by the remote movement of the saline front, must contribute to the observed tidal SP in the coastal borehole.

The arguments outlined above provide compelling evidence that a combination of EK and EED potential mechanisms are primarily responsible for the tidal SP observed in the borehole-referenced SP at the coastal site. However, the relative contribution of EK and EED potentials to the observed tidal SP needs to be investigated separately using numerical modeling.

4.5. Implications for SP Monitoring in Coastal Aquifers

Since tidal SP is caused by EK and EED potentials, borehole-referenced SP monitoring could aid aquifer management. SP could be used to characterize coastal aquifers through joint inversion with hydraulic data [*Soueid Ahmed et al*., 2014; *Straface et al*., 2007; *Chidichimo et al*., 2015; *Straface et al*., 2011], including determining aquifer transmissivity using tidal boreholes [*Carr and Van Der Kamp*, 1969; *Millham and Howes*, 1995; *Rotzoll and El-Kadi*, 2008; *Rotzoll et al*., 2013; *Trefry and Bekele*, 2004]. SP could also be used to determine dispersivity [*Revil and Jardani*, 2010; *Straface and De Biase*, 2013], allowing characterization of the saline transition zone

[*Abarca et al.*, 2007; *Kerrou and Renard*, 2010]. Finally, modeling suggests that the movement of the saline front may contribute to SP measured in remote boreholes [*Gulamali et al.*, 2011; *Jackson et al.*, 2012b]. Thus, SP could provide early warning of saline breakthrough. However, further research is required.

5. Conclusions

The main tidal constituents (M_2, the semidiurnal, principal lunar cycle and K_1, the diurnal, and principal lunar-solar cycle) were present in borehole-referenced SP data acquired at a coastal site, suggesting that SP responds to ocean tidal processes in the aquifer. No frequency components were found to be significant in borehole-referenced SP data acquired at an inland site. The M_2 component was observed in surface-referenced SP data but was less significant than the S_1 component which was driven by the diurnal temperature cycle. The M_2 component in surface-referenced SP is likely to be influenced by a combination of Earth, atmospheric and geomagnetic tides. These processes must be accounted for in surface measurements or surface-referenced borehole measurements of SP if diurnal or semidiurnal processes are of interest, even in studies conducted far from the coast. The analysis presented here demonstrates that borehole-referenced SP in coastal aquifers is primarily driven by ocean tidal process in the aquifer, implying that EK and EED potentials are the primary SP source mechanisms. Further work is required to understand the competing contributions of EK and EED potentials. However, an initial analysis suggests that EK is unlikely to be solely responsible for the observed tidal SP. The results suggest that SP may have multiple applications in coastal aquifers, including characterization and monitoring, and could form part of a borehole contamination early warning system.

Appendix A

The results from the PSD analysis of the hydrodynamic and SP data from the long-term monitoring experiment at the coastal site are presented here (Figures A1, A2, A3, A4, A5, A6).

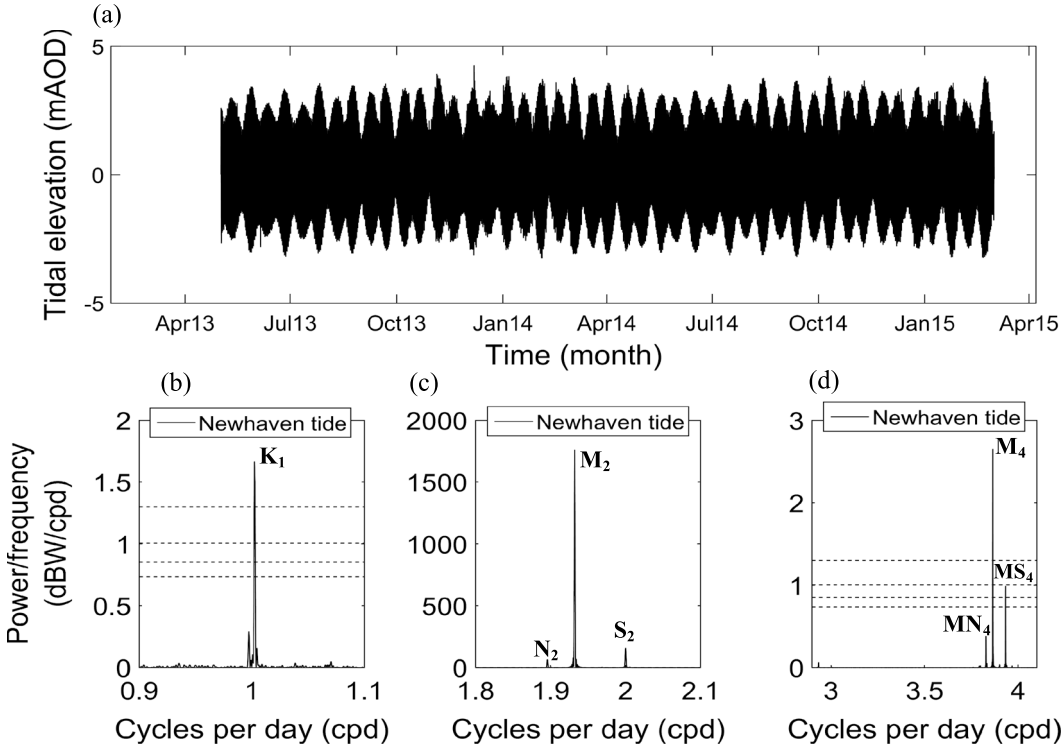

Figure A1. Long-term tidal gauge data from the coastal site. (a) Newhaven tidal gauge data. (b) PSD analysis of the tidal gauge data for diurnal signals. (c) PSD for semidiurnal signals. (d) PSD for 3–4 cycles per day.

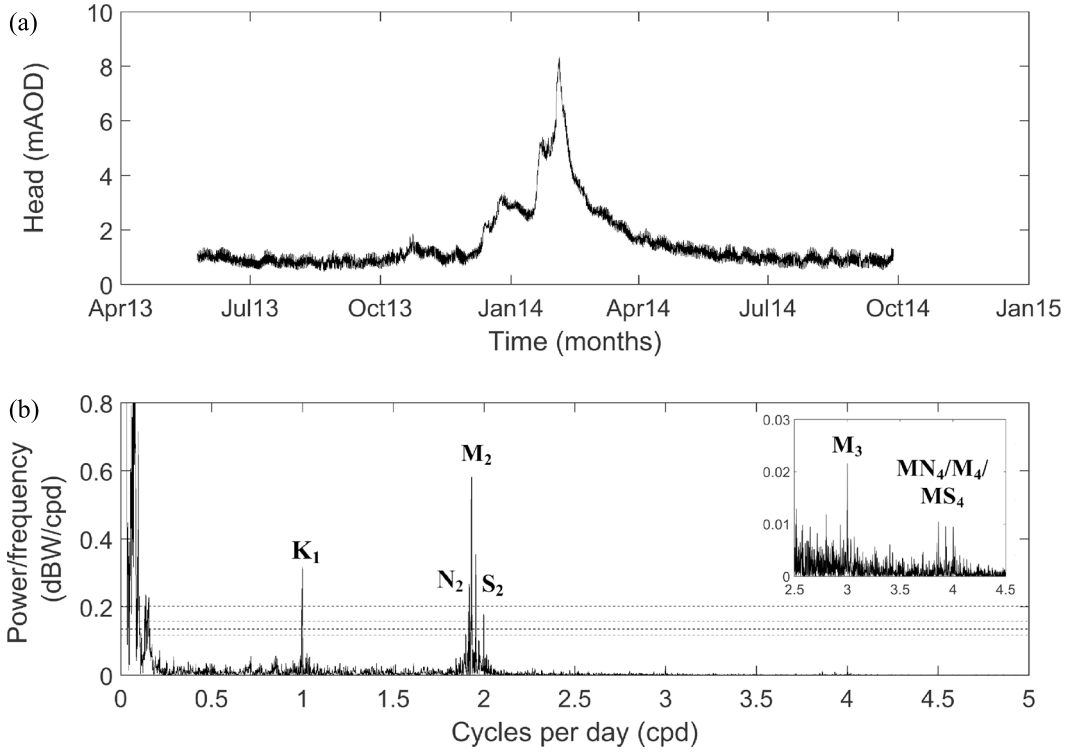

Figure A2. Long-term head data from the coastal site. (a) Borehole head. (b) PSD of head. The inset plot shows the components with a periodicity of 3–4 cycles per day.

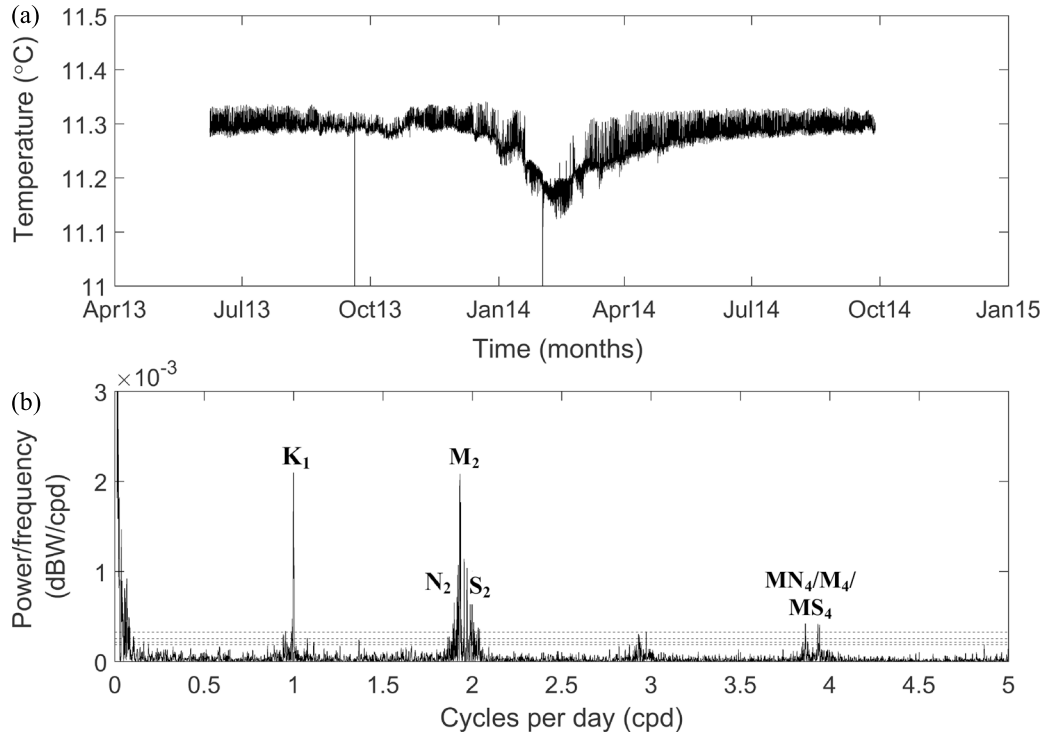

Figure A3. Long-term borehole temperature data from the coastal site. (a) Borehole temperature. (d) PSD of temperature.

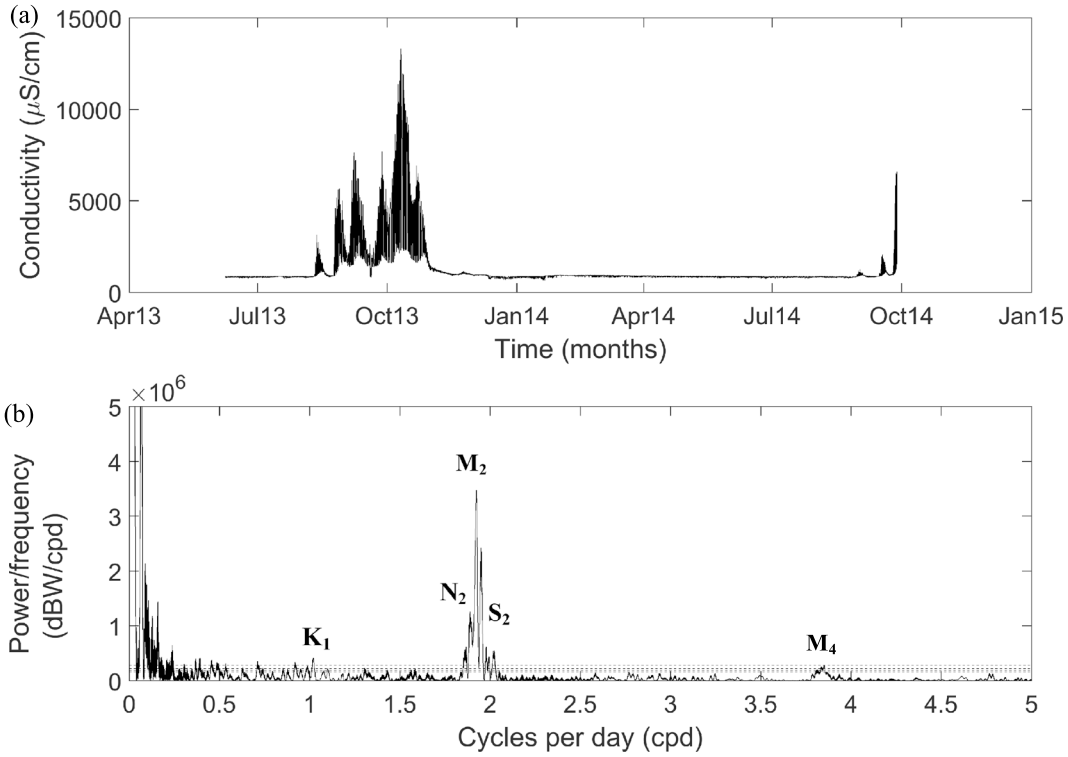

Figure A4. Long-term borehole FEC data from the coastal site. (a) Borehole FEC, note that on two occasions saline water entered the borehole and the conductivity increased. (b) PSD of FEC.

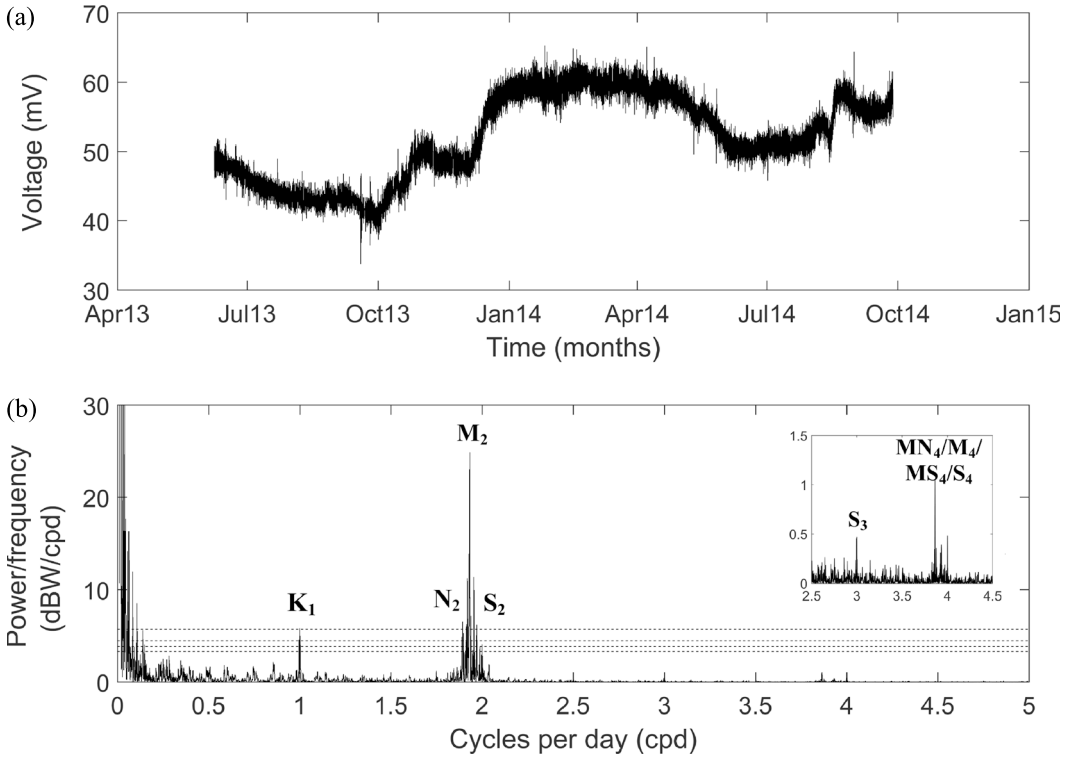

Figure A5. Long-term surface-referenced SP data from the coastal site. (a) Surface-referenced SP. (b) PSD of the surface-referenced SP (BH1-C-Ref-C). The inset plot shows the components with a periodicity of 3–4 cycles per day.

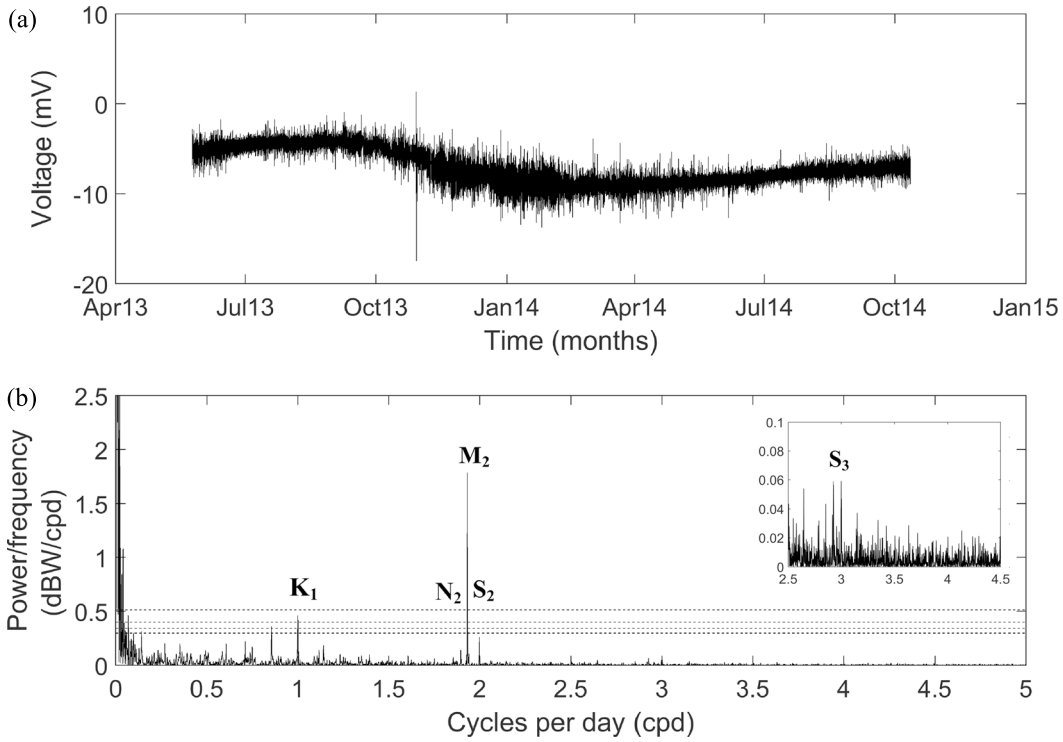

Figure A6. Long-term borehole-referenced SP data from the coastal site. (a) Borehole-referenced SP. (b) PSD of the borehole-referenced SP (BH1-C-BH13-C). The inset plot shows the components with a periodicity of 3–4 cycles per day.

Acknowledgments

MacAllister was supported by NERC CASE studentship NE/I018417/1. The authors would also like to thank Southern Water for access to the borehole at Saltdean. Atkins Global and Southern Water are thanked for funding installation of the equipment and for additional funding under the NERC studentship. The laboratory components of this work were carried out in the TOTAL Reservoir Physics Laboratory at Imperial College London, and their support is gratefully acknowledged. Jackson acknowledges partial support from TOTAL under the TOTAL Chairs program. The data supporting the conclusions of this work are available through the corresponding author.

References

Abarca, E., J. Carrera, X. Sanchez-Vila, and M. Dentz (2007), Anisotropic dispersive henry problem, *Adv. Water Resour.*, *30*, 913–926.

Adler, P. M., J.-F. Thovert, C. Jacquin, P. Morat, and J.-L. Le Mouel (1997), Electrical signals induced by the atmospheric pressure variations in unsaturated media, *Comp. R. De L'académie Des Sci. Sér. 2. Sci. De La Terre Et Des Planètes*, *324*, 711–718.

Agnew, D. C. (2007), 3.06—Earth tides, in *Treatise on Geophysics*, edited by G. Schubert, Elsevier, Amsterdam.

Allègre, V., A. Maineult, F. Lehmann, F. Lopes, and M. Zamora (2014), Self-potential response to drainage–imbibition cycles, *Geophys. J. Int.*, *197*(3), 1410–1424.

Apel, J. R. (1987), *Principles of Ocean Physics*, Elsevier Science, London.

Baptista, A. M., J. J. Westerink, and P. J. Turner (1989), Tides in the English Channel and Southern North Sea. A frequency domain analysis using model Tea-NL, *Adv. Water Resour.*, *12*, 166–183.

Bindoff, N., F. Lilley, and J. Filloux (1988), A separation of ionospheric and oceanic tidal components in magnetic fluctuation data, *J. Geomagn. Geoelectr.*, *40*, 1445–1467.

British Oceanographic Data Centre (2015), Uk tide gauge network [online]. British Oceanographic Data Centre. Available at Https://Www.Bodc.Ac.Uk/Data/Online_Delivery/Ntslf/ [Accessed 13/08/205 2015.]

Bolève, A., F. Janod, A. Revil, A. Lafon, and J. J. Fry (2011), Localization and quantification of leakages in dams using time-lapse self-potential measurements associated with salt tracer injection, *J. Hydrol.*, *403*, 242–252.

Bristow, R., R. Mortimore, and C. Wood (1997), Lithostratigraphy for mapping the Chalk of Southern England, *Proc. Geol. Assoc.*, *108*, 293–315.

Brown, G. M., and W. G. Woods (1971), Tidal influence on Earth currents at a coastal station, *J. Atmos. Terr. Phys.*, *33*, 289–293.

Bumpus, P. B., and S. E. Kruse (2014), Self-potential monitoring for hydrologic investigations in urban covered-karst terrain, *Geophysics*, *79*, B231–B242.

Butler, A. P., S. A. Mathias, A. J. Gallagher, D. W. Peach, and A. T. Williams (2009), Analysis of flow processes in fractured chalk under pumped and ambient conditions (UK), *Hydrogeol. J.*, *17*, 1849–1858.

Carr, P. A., and G. S. Van Der Kamp (1969), Determining aquifer characteristics by the tidal method, *Water Resour. Res.*, *5*, 1023–1031, doi:10.1029/WR005i005p01023.

Castermant, J., C. A. Mendonça, A. Revil, F. Trolard, G. Bourrié, and N. Linde (2008), Redox potential distribution inferred from self-potential measurements associated with the corrosion of a burden metallic body, *Geophys. Prospect.*, *56*, 269–282.

Chapman, S., and P. C. Kendall (1970), Sea tidal generation of electric currents and magnetic fields: Applications to five stations within the British Isles, *Planet. Space Sci.*, *18*, 1597–1605.

Chidichimo, F., M. De Biase, E. Rizzo, S. Masi, and S. Straface (2015), Hydrodynamic parameters estimation from self-potential data in a controlled full scale site, *J. Hydrol.*, *522*, 572–581.

Cochrane, N. A., and S. P. Srivastava (1974), Tidal influence on electric and magnetic fields recorded at coastal sites in Nova Scotia, Canada, *J. Atmos. Terr. Phys.*, *36*, 49–59.

Corwin, R. F. (1990), The self-potential method for environmental and engineering applications, *Geotech. Environ. Geophys.*, *1*, 127–145.

Cueto, M., D. Mcknight, and M. Herraiz (2003), Daily geomagnetic variations on the Iberian Peninsula, *Geophys. J. Int.*, *152*, 113–123.

Dai, A., and J. Wang (1999), Diurnal and semidiurnal tides in global surface pressure fields, *J. Atmos. Sci.*, *56*, 3874–3891.

de Franco, R., et al. (2009), Monitoring the saltwater intrusion by time lapse electrical resistivity tomography: The Chioggia test site (Venice Lagoon, Italy), *J. Appl. Geophys.*, *69*(3–4), 117–130.
Doodson, A. T. (1921), The harmonic development of the tide-generating potential, *Proc. R. Soc. Lond. Ser. A Contain. Pap. Math. Phys. Charact.*, *100*, 305–329.
Falgàs, E., J. Ledo, A. Marcuello, and P. Queralt (2009), Monitoring freshwater-seawater interface dynamics with audiomagnetotelluric data, *Near Surf. Geophys.*, *7*(5–6), 391–399.
Food and Agricultural Organisation (1997), *Seawater Intrusion in Coastal Aquifers: Guidelines for Study, Monitoring and Control*, Food And Agricultural Organisation Of The United Nations, Rome.
Forbes, J. M., et al. (1994), Semidiurnal tide in the 80–150 km region: An assimilative data analysis, *J. Atmos. Terr. Phys.*, *56*, 1237–1249.
Geller, M. A. (1970), An investigation of the lunar semidiurnal tide in the atmosphere, *J. Atmos. Sci.*, *27*, 202–218.
Gokhberg, M. B., Kolosnitsyn, N. I., and Lapshin, V. M. (2009), Electrokinetic effect in the near-surface layers of the Earth. Izvestiya, *Phys. Solid Earth*, *45*, 633–639.
Gulamali, M. Y., E. Leinov, and M. D. Jackson (2011), Self-potential anomalies induced by water injection into hydrocarbon reservoirs, *Geophysics*, *76*, F283–F292, doi:10.1190/1.3596010.
Hamilton, J. (1978), The quarter-diurnal tide in the English Channel, *Geophys. J. Int.*, *53*, 541–552.
Hart, A. M., C. D. Honebon, and W. G. V. Rosser (1983a), Local contributions to the M_2 lunar geomagnetic variations in the South West of England, *Physi. Earth Planet. Int.*, *32*, 60–64.
Hart, A. M., P. J. Krause, and W. G. V. Rosser (1983b), Possible contribution of leakage currents from the Atlantic Ocean to the magnetic-field variations observed in Devon, *Phys. Earth Planet. Int.*, *32*, 107–113.
Hewson-Browne, R. C. (1973), Magnetic effects of sea tides, *Phys. Earth Planet. Int.*, *7*, 167–186.
Jackson, M. D., A. P. Butler, and J. Vinogradov (2012a), Measurements of spontaneous potential in chalk with application to aquifer characterisation in the southern UK quarterly, *J. Eng. Geol. Hydrogeol.*, *45*, 457–471.
Jackson, M. D., M. Y. Gulamali, E. Leinov, J. H. Saunders, and J. Vinogradov (2012b), Spontaneous potentials in hydrocarbon reservoirs during waterflooding: Application to water-front monitoring, *SPE J.*, *17*, 53–69.
Jones, H. K., and N. S. Robins (1999), *The Chalk Aquifer of the South Downs*, British Geological Survey, Keyworth, Nottingham.
Jougnot, D., N. Linde, A. Revil, and C. Doussan (2012), Derivation of soil-specific streaming potential electrical parameters from hydrodynamic characteristics of partially saturated soils, *Vadose Zone J.*, *11*(1), 15.
Jougnot, D., N. Linde, E. B. Haarder, and M. C. Looms (2015), Monitoring of saline tracer movement with vertically distributed self-potential measurements at the hobe agricultural test site, Voulund, Denmark, *J. Hydrol.*, *521*, 314–327.
Kang, H. J., I. K. Cho, J. H. Kim, H. H. Yong, S. H. Song, and Y. G. Park (2014), SP monitoring at a sea dike, *Near Surf. Geophys.*, *12*, 83–92.
Karl, J. H. (1989), 11—Power spectral estimation, in *Introduction to Digital Signal Processing*, edited by J. H. Karl, Academic Press, San Diego, Calif.
Kendall, P. C., and S. Chapman (1970), Model calculations on sea tidal generation of electric currents and magnetic fields, *Quart. J. Mech. Appl. Math.*, *23*, 535–547.
Kerrou, J., and P. Renard (2010), A numerical analysis of dimensionality and heterogeneity effects on advective dispersive seawater intrusion processes, *Hydrogeol. J.*, *18*, 55–72.
Kuan, W. K., G. Jin, P. Xin, C. Robinson, B. Gibbes, and L. Li (2012), Tidal influence on seawater intrusion in unconfined coastal aquifers, *Water Resour. Res.*, 48, W02502, doi:10.1029/2011WR010678.
Kulessa, B. (2003), Cross-coupled flow modeling of coincident streaming and electrochemical potentials and application to subglacial self-potential data, *J. Geophys. Res.*, 108(B8), 2381, doi:10.1029/2001JB001167.
Kulessa, B., B. Hubbard, G. H. Brown, and J. Becker (2003), Earth tide forcing of glacier drainage, *Geophys. Res. Lett.*, *30*(1), 1011, doi:10.1029/2002GL015303.
Kumpel, H. J. (1997), Tides in water saturated rock, in *Tidal Phenomena*, edited by H. Wilhelm, W. Zurn, and H. G. Wenzel, Springer, Berlin.
Lilley, F. E. M., and R. L. Parker (1976), Magnetic daily variations compared between the east and west coasts of Australia, *Geophys. J. Int.*, *44*, 719–724.
Linde, N., J. Doetsch, D. Jougnot, O. Genoni, Y. Dürst, B. J. Minsley, T. Vogt, N. Pasquale, and J. Luster (2011), Self-potential investigations of a gravel bar in a restored river corridor, *Hydrol. Earth Syst. Sci.*, *15*, 729–742.
Lindzen, R., and S. Chapman (1969), Atmospheric tides, *Space Sci. Rev.*, *10*, 3–188.
Lomb, N. R. (1976), Least-squares frequency analysis of unequally spaced data, *Astrophys. Space Sci.*, *39*, 447–462.
Love, J. J., and E. J. Rigler (2014), The magnetic tides of Honolulu, *Geophys. J. Int.*, *197*, 1335–1353.
Maineult, A., Y. Bernabe, and P. Ackerer (2004), Electrical response of flow diffusion and advection in a laboratory sand box, *Vadose Zone J.*, *3*, 1180–1192.
Maineult, A., E. Strobach, and J. Renner (2008), Self-potential signals induced by periodic pumping tests, *J. Geophys. Res.*, *113*, B01203, doi:10.1029/2007JB005193.
Mariethoz, G., N. Linde, D. Jougnot, and H. Rezaee (2015), Feature-preserving interpolation and filtering of environmental time series, *Environ. Modell. Software*, *72*, 71–76.
Mathias, S. A., A. P. Butler, D. W. Peach, and A. T. Williams (2007), Recovering tracer test input functions from fluid electrical conductivity logging in fractured porous rocks, *Water Resour. Res.*, *43*, W07443, doi:10.1029/2006WR005455.
Maus, S., and A. Kuvshinov (2004), Ocean tidal signals in observatory and satellite magnetic measurements, *Geophys. Res. Lett.*, *31*, L15313, doi:10.1029/2004GL020090.
Millham, N. P., and B. L. Howes (1995), A comparison of methods to determine K in a shallow coastal aquifer, *Ground Water*, *33*, 49–57.
Orihara, Y., M. Kamogawa, T. Nagao, and S. Uyeda (2012), Variations of geoelectric potential differences associated with an anomalous volumetric strain change in the region of expected Tokai Earthquake, Japan, *Nat. Hazards Earth Syst. Sci.*, *12*, 121–127.
Osgood, C., W. G. V. Rosser, and N. J. W. Webber (1970), Electric and magnetic fields associated with sea tides in the English Channel, *Phys. Earth Planet. Int.*, *4*, 65–77.
Palshin, N. A., L. L. Vanyan, and P. Kaikkonen (1996), On-shore amplification of the electric field induced by a coastal sea current, *Phys. Earth Planet. Int.*, *94*, 269–273.
Perrier, F. E., et al. (1997), A one-year systematic study of electrodes for long period measurements of the electric field in geophysical environments, *J. Geomagn. Geoelectric.*, *49*, 1677–1696.
Perrier, F., M. Trique, B. Lorne, J. P. Avouac, S. Hautot, and P. Tarits (1998), Electric potential variations associated with yearly lake level variations, *Geophys. Res. Lett.*, *25*, 1955–1958, doi:10.1029/98GL01139.
Perrier, F., M. Trique, J. Aupiais, U. Gautam, and P. Shrestha (1999), Electric potential variations associated with periodic spring discharge in western Nepal, *Comptes R. De L Acad. Des Sci. Ser. Ii Fascicule A-Sci. De La Terre Et Des Planetes*, *328*, 73–79.

Revil, A. (1999), Ionic diffusivity electrical conductivity membrane and thermoelectric potentials in colloids and granular porous media: A unified model, *J. Colloid Interface Sci.*, *212*, 503–522.
Revil, A., and A. Jardani (2010), Stochastic inversion of permeability and dispersivities from time lapse self-potential measurements: A controlled sandbox study, *Geophys. Res. Lett.*, *37*, L11404, doi:10.1029/2010GL043257.
Revil, A., C. Gevaudan, N. Lu, and A. Maineult (2008), Hysteresis of the self-potential response associated with harmonic pumping tests, *Geophys. Res. Lett.*, *35*, L16402, doi:10.1029/2008GL035025.
Rojstaczer, S., and F. S. Riley (1990), Response of the water level in a well to Earth tides and atmospheric loading under unconfined conditions, *Water Resour. Res.*, *26*, 1803–1817, doi:10.1029/WR026i008p01803.
Rosas-Carbajal, M., N. Linde, T. Kalscheuer, and J. A. Vrugt (2013), Two-dimensional probabilistic inversion of plane-wave electromagnetic data: Methodology, model constraints and joint inversion with electrical resistivity data, *Geophys. J. Int.*, *482*.
Rosser, W. G. V., and D. M. Schlapp (1990), Geomagnetic lunar variations due to the ocean dynamo measured at European observatories, *Geophys. J. Int.*, *103*, 257–260.
Rotzoll, K., and A. I. El-Kadi (2008), Estimating hydraulic properties of coastal aquifers using wave setup, *J. Hydrol.*, *353*, 201–213.
Rotzoll, K., S. B. Gingerich, J. W. Jenson, and A. I. El-Kadi (2013), Estimating hydraulic properties from tidal attenuation in the northern Guam Lens Aquifer, territory of Guam, USA, *Hydrogeol. J.*, *21*, 643–654.
Scargle, J. D. (1982), Studies in astronomical time series analysis. II—Statistical aspects of spectral analysis of unevenly spaced data, *Astrophys. J.*, *263*, 835–853.
Schürch, M., and D. Buckley (2002), Integrating geophysical and hydrochemical borehole-Log measurements to characterize the Chalk aquifer, Berkshire, United Kingdom, *Hydrogeol. J.*, *10*, 610–627.
Silvion (2013), Type We200 reference electrode for permananet installation in soil. In: Silvion (Ed.) Http://Www.Silvion.Co.Uk/Pdf/1426002349we200-R6.Pdf. http://Www.Silvion.Co.Uk/: Silvion.
Silvion (2015), Type We300 Low Ion reference electrode for use in potable water. In: Silvion (Ed.) Http://Www.Silvion.Co.Uk/Pdf/1426002360we300-R6.Pdf. http://Www.Silvion.Co.Uk/: Silvion.
Soueid Ahmed, A. S., A. Jardani, A. Revil, and J. P. Dupont (2014), Hydraulic conductivity field characterization from the joint inversion of hydraulic heads and self-potential data, *Water Resour. Res.*, *50*, 3502–3522, doi:10.1002/2013WR014645.
Straface, S., and M. De Biase (2013), Estimation of longitudinal dispersivity in a porous medium using self-potential signals, *J. Hydrol.*, *505*, 163–171.
Straface, S., C. Fallico, S. Troisi, E. Rizzo, and A. Revil (2007), An inverse procedure to estimate transmissivity from heads and SP signals, *Ground Water*, *45*, 420–8.
Straface, S., F. Chidichimo, E. Rizzo, M. Riva, W. Barrash, A. Revil, M. Cardiff, and A. Guadagnini (2011), Joint inversion of steady-state hydrologic and self-potential data for 3D hydraulic conductivity distribution at the boise hydrogeophysical research site, *J. Hydrol.*, *407*, 115–128.
Trauth, M. H. (2010), *Matlab® Recipes for Earth Sciences*, 3rd ed., Springer, Berlin.
Trefry, M. G., and E. Bekele (2004), Structural characterization of an island aquifer via tidal methods, *Water Resour. Res.*, *40*, W01505, doi:10.1029/2003WR002003.
Trique, M., F. Perrier, T. Froidefond, and J. P. Avouac (2002), Fluid flow near reservoir lakes inferred from the spatial and temporal analysis of the electric potential, *J. Geophys. Res.*, *107*, B102239, doi:10.1029/2001JB000482.
Van Weert, F., J. Van Der Gun, and J. Reckman (2009), *Global Overview of Saline Groundwater Occurrence And Genesis*, UNESCO And WMO, Utrectht, The Netherlands.
Vial, F., and J. M. Forbes (1994), Monthly simulations of the lunar semi-diurnal tide, *J. Atmos. Terr. Phys.*, *56*, 1591–1607.
Walters, R. A. (1987), A model for tides and currents in the English Channel and southern North Sea, *Adv. Water Resour.*, *10*, 138–148.
Werner, A. D., D. Jakovovic, and C. T. Simmons (2009), Experimental observations of saltwater up-coning, *J. Hydrol.*, *373*, 230–241.
Wheater, H. S., D. Peach, and A. Binley (2007), Characterising groundwater-dominated lowland catchments: The UK lowland catchment research programme (LOCAR), *Hydrol. Earth Syst. Sci. Discuss.*, *11*, 108–124.
Williams, A., J. Bloomfield, K. Griffiths, and A. Butler (2006), Characterising the vertical variations in hydraulic conductivity within the Chalk aquifer, *J. Hydrol.*, *330*, 53–62.
Woods, M. A. (2006), UK Chalk Group stratigraphy determined (Cenomanian–Santonian) determined from borehole geophysical logs, *Quart. J. Eng. Geol. Hydrogeol.*, *39*, 83–96.
Zhou, Q. L., J. Bear, and J. Bensabat (2005), Saltwater upconing and decay beneath a well pumping above an interface zone, *Trans. Porous Media*, *61*, 337–363.